



Oxygen vacancies-modified S-scheme heterojunction of Bi-doped $\text{La}_2\text{Ti}_2\text{O}_7$ and La-doped $\text{Bi}_4\text{Ti}_3\text{O}_{12}$ to improve the NO gas removal avoiding NO_2 product

Li Lv^{a,b,c}, Lin Lei^a, Qi-Wen Chen^c, Cheng-Li Yin^c, Huiqing Fan^{a,*}, Jian-Ping Zhou^{c,*}

^a State Key Laboratory of Solidification Processing, School of Materials Science and Engineering, Northwestern Polytechnical University, Xi'an 710072, People's Republic of China

^b School of General Education, Xi'an Mingde Institute of Technology, Xi'an 710124, People's Republic of China

^c School of Physics and Information Technology, Shaanxi Normal University, Xi'an 710119, People's Republic of China

ARTICLE INFO

Keywords:

Photocatalysis
NO removal
Heterojunction
Oxygen vacancy
Doping

ABSTRACT

Monoclinic phase $\text{La}_2\text{Ti}_2\text{O}_7$ and orthorhombic phase $\text{Bi}_4\text{Ti}_3\text{O}_{12}$ with layered crystal structure constructed by the perovskite slab were widely used in photocatalysis. Their electronic structures are the most crucial factor in high photocatalytic activity. Bi-doped $\text{La}_2\text{Ti}_2\text{O}_7$ gradually converts to La-doped $\text{Bi}_4\text{Ti}_3\text{O}_{12}$ with the incorporation of bismuth ions, and the two phases build an S-scheme heterojunction. More oxygen vacancies were introduced into the S-scheme heterojunction after heat treatment in a nitrogen atmosphere. The 0.1BTO/LTO-OV sample exhibits the largest NO removal efficiency of 52% and only 5.6 ppb NO_2 intermediate generation. The improved NO removal efficiency was ascribed to the synergistic effect of oxygen vacancies, doping and heterojunction, providing a new insight into the photocatalytic NO removal. The photocatalytic mechanism was eventually proposed on the basis of trapping experiments.

1. Introduction

Modern industry brings about a series of air pollution to severely deteriorate the sustainable development of human world. The various air pollutants include carbon dioxide (CO_2), nitrogen oxide (NO_x), sulfur dioxide (SO_2) and volatile organic compounds (VOCs) [1]. Among them, nitric oxide (NO) is the most dangerous pollutant because it can cause atmospheric environmental problems, endanger human health and destroy the environment ecosystem. But the NO concentration in atmosphere increases continuously in the past decades because of the rapid development of industry and transportation. Therefore, it is urgent to develop green and sustainable strategies for NO removal. Semiconductor photocatalytic technology has stood out in the degradation of ppb concentrations of NO due to its high efficiency, economical cost and environmental protection. However, a certain amount of NO_2 gas is inevitable as the intermediate product during the photocatalytic degradation of NO gas. In fact, the intermediate NO_2 ought to be also

removed as far as possible during the NO treatments since NO_2 is even more toxic than NO [2,3].

Heterojunctions combining two photocatalysts are demonstrated to effectively improve photocatalytic performance by relieving the recombination of photogenerated carriers in a single photocatalyst [4, 5]. S-scheme heterojunction composed of a reduction semiconductor and an oxidation semiconductor was recently proposed with suitably staggered band configurations. The oxidation photocatalyst owns a more positive valance band position, while the reduction photocatalyst has a more negative conduction band position [6,7]. The S-scheme heterojunctions retain the redox capability of both semiconductors in comparison with conventional type-II heterojunctions and enhance the charge transfer at interface by the built-in electric field to promote photocatalytic efficiency. Oxygen vacancies, with abundant localized electrons, have been demonstrated to serve as electron trap centers that can effectively capture and activate inert gas molecules such as CO_2 , N_2 and NO gas [3,8–10]. At the same time, the oxygen vacancy with

* Corresponding authors.

E-mail addresses: hqfan@nwpu.edu.cn (H. Fan), zhoujp@snnu.edu.cn (J.-P. Zhou).

¹ ORCID: 0000-0002-1405-9279

² ORCID: 0000-0003-0807-1404

³ ResearcherID: AGE-2972-2022

appropriate concentration can also improve light absorption and promote the separation of photogenerated electrons and holes [3].

The perovskite $\text{La}_2\text{Ti}_2\text{O}_7$ is built by a stack of four layers of corner-sharing $[\text{TiO}_6]$ octahedron along the c axis, linked to a neighboring slab by lanthanum cations lying near the boundary [11,12]. The perovskite $\text{La}_2\text{Ti}_2\text{O}_7$ possesses many unique properties, such as superior thermal stability, good electron mobility, high conductivity and ferroelectric property. Therefore, it has been investigated as a functional material in various applications like photocatalytic hydrogen evolution [13], Lithium-Ion Batteries [14], sensors [15], storage devices [16] and photodegradation [17,18]. However, its large band gap (~ 3.6 eV) prevents photocatalytic efficiency in visible light. As an ionic conductor at room temperature, $\text{La}_2\text{Ti}_2\text{O}_7$ shows a high ion mobility due to the ions on A sites, which can easily migrate to thermodynamic equilibrium locations. Hence, $\text{La}_2\text{Ti}_2\text{O}_7$ provides a good parent material for chemical substitutions maintaining the original perovskite structure. The ions doped on the A sites tend to be segregated at locations with lower formation energy. Bi^{3+} cation is a good candidate to dope $\text{La}_2\text{Ti}_2\text{O}_7$ photocatalyst because the intrinsic polarization induced by the Bi 6s lone pair electron is beneficial to the separation of photogenerated electrons and holes [19]. The ferroelectric bismuth titanate ($\text{Bi}_4\text{Ti}_3\text{O}_{12}$), as a member of the Aurivillius family, is constructed by alternate stacking of $(\text{Bi}_2\text{O}_2)^{2+}$ layers and perovskite $(\text{Bi}_2\text{Ti}_3\text{O}_{10})^{2-}$ layers along the c axis [20–22], which form an internal electric field to promote the separation of photogenerated electrons and holes, thereby enhancing the photocatalytic activity. Nevertheless, the large band gap of $\text{Bi}_4\text{Ti}_3\text{O}_{12}$ (~ 3 eV) limits its light absorption, reducing the photocatalytic performance as a photocatalyst. Foreign element doping can effectively improve the photocatalytic activity of semiconductors by introducing dopant energy levels in the bandgap. And carrier trapping centers efficiently prevent the recombination of photogenerated electrons and holes [21,23]. Considering the chemical state and ionic radius, we equivalently doped La^{3+} ions (1.032 \AA) to substitute Bi^{3+} ions (1.03 \AA) in $\text{Bi}_4\text{Ti}_3\text{O}_{12}$.

In this study, we prepared S-scheme heterojunctions of Bi-doped $\text{La}_2\text{Ti}_2\text{O}_7$ and La-doped $\text{Bi}_4\text{Ti}_3\text{O}_{12}$. Then, oxygen vacancies were introduced into the heterojunction to promote photocatalytic performance. The improved NO gas removal avoiding NO_2 secondary pollution was systematically researched. This work provides hopeful insights into designing oxygen vacancies-modified and metal ion-doped S-scheme heterojunction with highly efficient photocatalysis.

2. Experimental details

2.1. Sample preparation

The Bi-doped $\text{La}_2\text{Ti}_2\text{O}_7$, La-doped $\text{Bi}_4\text{Ti}_3\text{O}_{12}$ and their heterojunctions were prepared by a normal hydrothermal method [18]. All the raw reagents were analytically pure. The appropriate molar quantities of $\text{La}(\text{NO}_3)_3 \cdot 6\text{H}_2\text{O}$, $\text{Bi}(\text{NO}_3)_3 \cdot 5\text{H}_2\text{O}$ and $\text{Ti}(\text{SO}_4)_2$ were dissolved in deionized water under magnetic stirring until a clear aqueous solution. 1 mol KOH solution was dropped into the above solution to form a white precipitation mixture. The mixture was stirred for 30 min and then sealed in a 30 mL Teflon-lined stainless-steel autoclave to react at 220°C for 36 h. After reaction, the resulting powders were repeatedly washed several times with deionized water and then dried at 80°C for 12 h to get white powders. The samples with different Bi/(La+Bi) molar ratios of 0.01, 0.05, 0.1, 0.2, 0.3 and 0.4 are denoted as 0.01BLTO, 0.05BTO/LTO, 0.1BTO/LTO, 0.2BTO/LTO, 0.3BTO/LTO and 0.4LBTO, respectively.

1 g composite 0.1BTO/LTO power and 4 g NaBH_4 were ground together for 30 min in an agate mortar. Then, the composite powers were put in an open crucible to heat at 350°C for 1 h under the 100 mL/min flow of N_2 gas. After heat treatment, the resulting powders were repeatedly washed several times with deionized water and then dried at 80°C for 10 h to get gray powder, which was denoted as 0.1BTO/LTO-OV.

2.2. Measurements

The crystal structure of the samples was identified by an X-ray diffractometer (XRD, D/Max2550, Rigaku, $\text{CuK}\alpha$ radiation, accelerating voltage of 40 kV, applied current of 100 mA and scan rate of $5^\circ/\text{min}$) and Raman spectroscopy (Bruker Optics Senterra, laser wavelength of 532 nm and power of 2 mW). The powder morphology was observed by a field emission scanning electron microscope (FESEM, Nova Nano SEM 450). The crystal characteristics were further determined by field emission transmission electron microscopy (TEM, Talos F200i) combined with selected area electron diffraction (SAED). X-ray photoelectron spectroscopy (XPS) was measured with an instrument ESCALAB 250Xi (Kratos Analytical Ltd, Japan). All binding energies were calibrated with C 1s peak of adventitious carbon at 284.6 eV. UV–vis absorption spectra were recorded by a Lambda 950 UV–vis-NIR spectrophotometer (Perkin-Elmer, USA) in the wavelength range of 200 – 800 nm. The Mott-Schottky, photocurrent and electrochemical impedance were measured with an electrochemical workstation (CHI660E, Chenhua Instrument Co., Shanghai, China). Specific surface areas of the samples were measured with nitrogen adsorption-desorption isotherms at 77 K by a Micromeritics ASAP 2010 system after being preheated at 120°C for 12 h in a vacuum. The Fourier transform infrared (FT-IR) spectra were recorded on a Tensor27 spectrophotometer (Bruker, Germany) between 400 and 4000 cm^{-1} . The in situ electron spin resonance (ESR) signals were measured by a Bruker EMXplus spectrometer to detect the free radicals by mixing the as-prepared samples with 25 mM of 5,5'-dimethyl-1-pyrroline n-oxide (DMPO) solution and 2,2,6,6-tetramethylpiperidine (TEMP) trapping agent.

The photocatalytic activity of samples was evaluated by NO removal at ambient temperature in a continuous flowing NO gas with ppb level. 0.1 g sample was evenly dispersed in a glass dish (10 cm in diameter) via deionized water and ultrasonic treatment for 10 min, then dried under 60°C in the oven for 12 h. The photo-oxidative NO removal was performed in a quartz reactor (4.5 L , $10 \times 30 \times 15 \text{ cm}$) under irradiation of a 300 W Xenon lamp, which is 20 cm above the glass dish. The concentration of NO gas was recorded by a NO- NO_2 - NO_x analyzer (42i, Thermo Scientific) per minute. An entire measurement was conducted at room temperature and relative humidity of $30 \pm 5\%$. After the adsorption-desorption balance was achieved, the sample was illuminated.

The removal rate (η) of NO was calculated with Eq. (1).

$$\eta = 1 - (C/C_0) \times 100\% \quad (1)$$

where C is the NO concentration at a given time and C_0 is the initial concentration of NO with ppb. In the trapping experiments, 10 mg KI, $\text{K}_2\text{Cr}_2\text{O}_7$, β -carotene and PBQ and 10 mL of IPA were separately mixed with 0.1 g photocatalyst powder in 15 mL deionized water under sonication for 15 min and then, deposited onto the glass substrates for measurement.

The processes of adsorption and reaction of NO over 0.1BTO/LTO-OV were investigated using an in situ diffuse reflectance infrared Fourier-transform spectroscopy (DRIFTS) (TENSOR II, Bruker). The sample was sealed and degassed in a specimen chamber with high-purity helium (He) gas for 1 h to remove the air and impurities on catalyst surface. Subsequently, NO and O_2 were admitted into the reaction chamber and then spectra were recorded every two minutes in the dark and under illumination to research the adsorption and reaction processes.

2.3. Computational calculation

The formation energies and electronic structures of the single-phase doped materials were calculated by the Vienna ab initio simulation package program (VASP) [24] embedded in MedeA® software [25].

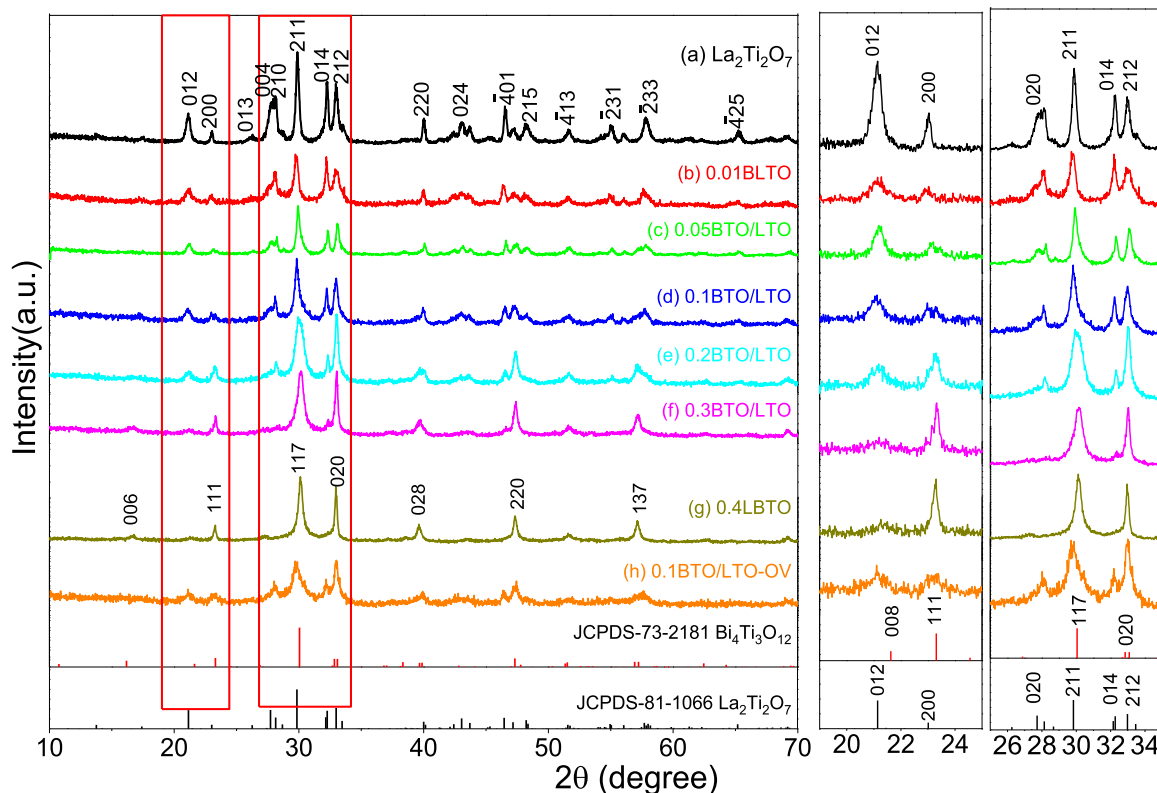


Fig. 1. XRD patterns of (a) pure $\text{La}_2\text{Ti}_2\text{O}_7$, (b) Bi-doped $\text{La}_2\text{Ti}_2\text{O}_7$, (c – f) heterojunctions, (g) La-doped $\text{Bi}_4\text{Ti}_3\text{O}_{12}$ and (h) 0.1BTO/LTO-OV, and their enlarged patterns near 22° and 30° .

Projector augmented wave potentials [26] were employed during calculations based on the density functional theory and generalized gradient approximation (GGA) with the Perdew-Burke-Ernzerhof (PBE) functional [27] to describe the interactions. The default cutoff energy of plane wave is 450 eV, and the electronic iteration convergence criterion is that the energy of each two-step iteration is ultimately less than 1×10^{-4} eV. The required k -spacing in reciprocal space is $0.3/\text{\AA}$, and the optimized structure meets the criterion of 0.02 eV/ \AA .

3. Results and discussions

3.1. Structural and morphological analysis

The crystal structure of photocatalysts was characterized by XRD as shown in Fig. 1. The pure $\text{La}_2\text{Ti}_2\text{O}_7$ has a monoclinic structure with space group $\text{P}2_1(4)$, $a = 7.81 \text{ \AA}$, $b = 5.55 \text{ \AA}$, $c = 13.02 \text{ \AA}$ and $\beta = 98.43^\circ$ (JCPDS No. 81–1066). The ionic radius of La^{3+} (103.2 pm) is close to that of Bi^{3+} (103 pm), providing a possibility to replace La^{3+} cations with Bi^{3+} cations in the $\text{La}_2\text{Ti}_2\text{O}_7$ lattice. The sample keeps $\text{La}_2\text{Ti}_2\text{O}_7$ single phase at low $\text{Bi}/(\text{La} + \text{Bi})$ molar ratio of 0.01 to be Bi-doped $\text{La}_2\text{Ti}_2\text{O}_7$ powders. $\text{Bi}_4\text{Ti}_3\text{O}_{12}$ phase appears with the increase in $\text{Bi}/(\text{La} + \text{Bi})$ molar ratio, and the $\text{La}_2\text{Ti}_2\text{O}_7$ peaks gradually weaken until disappear to become the orthorhombic $\text{Bi}_4\text{Ti}_3\text{O}_{12}$ phase with space group Fmmm , $a = 5.46 \text{ \AA}$, $b = 5.44 \text{ \AA}$ and $c = 33.17 \text{ \AA}$ (JCPDS No. 73–2181). The samples keep the coexistence of monoclinic and orthorhombic phases at the $\text{Bi}/(\text{La} + \text{Bi})$ molar ratios of 0.05, 0.1, 0.2 and 0.3. The La-doped $\text{Bi}_4\text{Ti}_3\text{O}_{12}$ single phase is obtained at the molar ratio of 0.4. The phase transition can be attributed to the doping-induced lattice distortion and tilting of octahedral by the incorporation of bismuth ions during the hydrothermal process [14]. The 0.1BTO/LTO-OV sample still keeps the same phases with 0.1BTO/LTO after introducing oxygen vacancies. However, its peak intensity becomes weak, indicating poor crystallinity caused by the oxygen vacancies, which will supply more

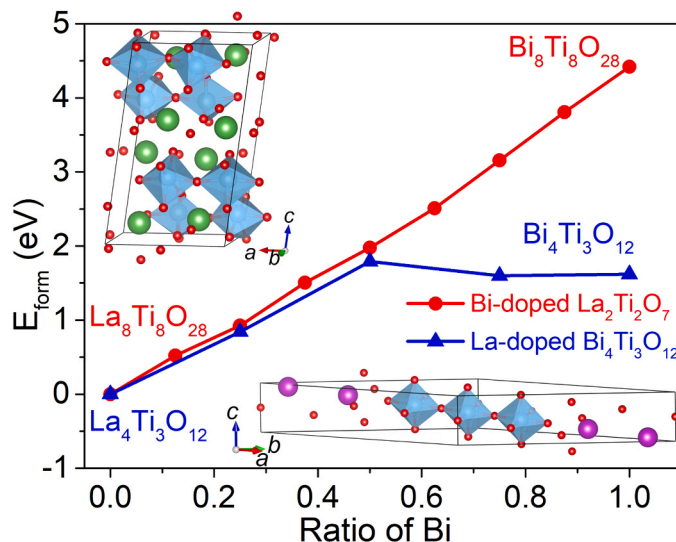


Fig. 2. Formation energy of $\text{La}_2\text{Ti}_2\text{O}_7$ and $\text{Bi}_4\text{Ti}_3\text{O}_{12}$ crystal structures with relative content of Bi in the doping process. The insets show the structural models used for calculation.

active sites during the photocatalytic reaction.

We calculated the formation energy of Bi-doped $\text{La}_2\text{Ti}_2\text{O}_7$ and La-doped $\text{Bi}_4\text{Ti}_3\text{O}_{12}$ to understand the phase change by density functional theory. The formation energy of doping materials is expressed as [28].

$$E_{\text{form}} = E_{\text{dope}} - E_{\text{bulk}} - n\mu_{\text{M}} + n\mu_{\text{N}} \quad (2)$$

where E_{dope} and E_{bulk} are the total energy after and before doping an atom, respectively. μ_{M} is the chemical potential of doping element, and

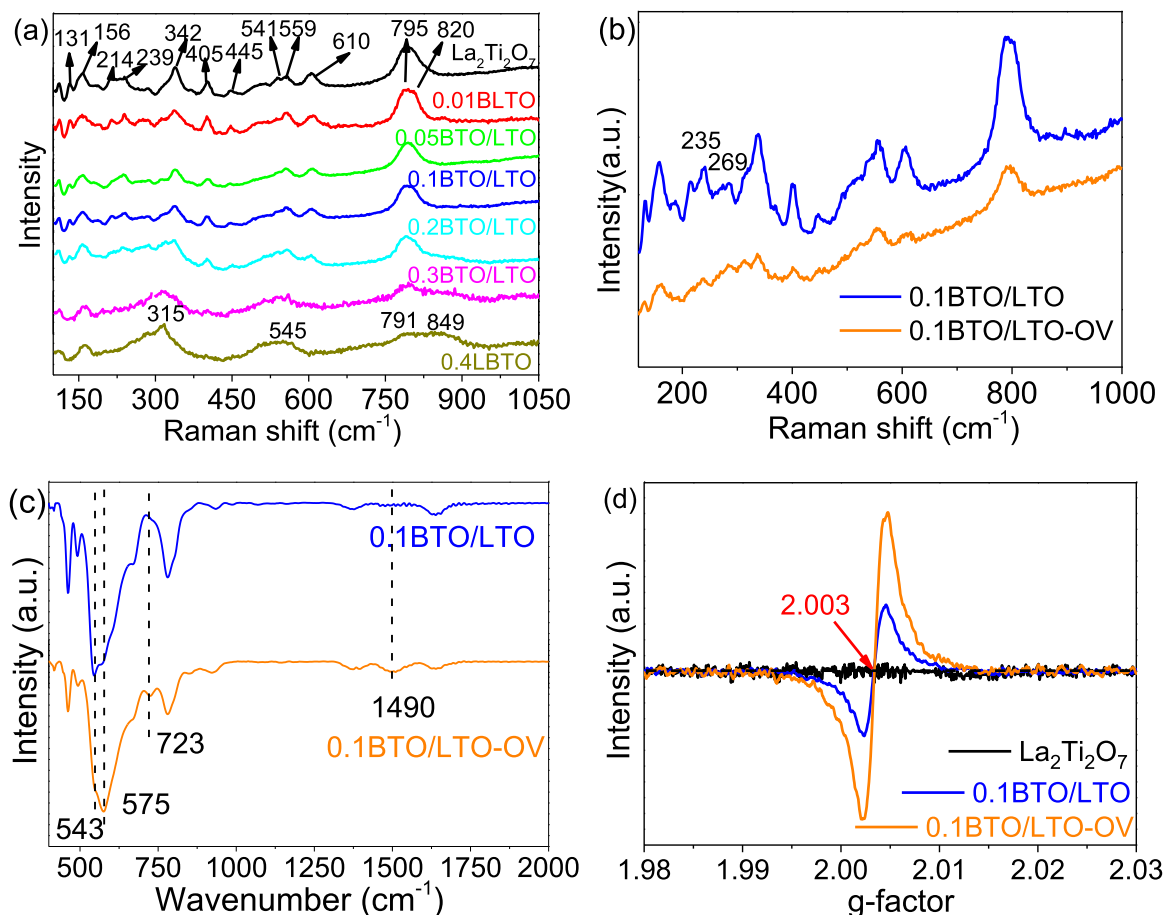


Fig. 3. (a) Raman spectra of pure $\text{La}_2\text{Ti}_2\text{O}_7$, Bi-doped $\text{La}_2\text{Ti}_2\text{O}_7$, La-doped $\text{Bi}_4\text{Ti}_3\text{O}_{12}$ and heterojunctions. (b) Raman spectra and (c) FT-IR spectra of 0.1BTO/LTO and 0.1BTO/LTO-OV. (d) ESR spectra of $\text{La}_2\text{Ti}_2\text{O}_7$, 0.1BTO/LTO and 0.1BTO/LTO-OV for comparison.

μ_N is the chemical potential of substituted atom. n is the number of substitutions. The chemical potential μ_M is obtained by the corresponding metal oxide with the following method

$$\mu_M = (\mu_{\text{M}_a\text{O}_b} - b\mu_{\text{O}})/a \quad (3)$$

where $\mu_{\text{M}_a\text{O}_b}$ represents the chemical potential of the corresponding metal oxide, and $\mu_{\text{O}} = \mu_{\text{O}_2}/2$ is the chemical potential of oxygen. Then, we get $\mu_{\text{Bi}} = -6.953$ eV and $\mu_{\text{La}} = -13.603$ eV.

Fig. 2 shows the formation energies of Bi-doped $\text{La}_2\text{Ti}_2\text{O}_7$ and La-doped $\text{Bi}_4\text{Ti}_3\text{O}_{12}$. The formation energy of $\text{La}_2\text{Ti}_2\text{O}_7$ increases with the Bi doping content, meaning La ions are difficultly substituted with Bi ions in the $\text{La}_2\text{Ti}_2\text{O}_7$ lattice. The formation energy of $\text{Bi}_4\text{Ti}_3\text{O}_{12}$ is steady at low La doping content and decreases at high La content, suggesting La ions easily enter into the $\text{Bi}_4\text{Ti}_3\text{O}_{12}$ lattice to replace Bi ions. This confirms the XRD results that the $\text{Bi}_4\text{Ti}_3\text{O}_{12}$ phase appears at a low Bi/(La+Bi) molar ratio of 0.05 due to the low Bi doping content in $\text{La}_2\text{Ti}_2\text{O}_7$ phase and the powder retains La-doped $\text{Bi}_4\text{Ti}_3\text{O}_{12}$ phase at a Bi/(La+Bi) molar ratio of 0.4 due to the high La doping content in $\text{Bi}_4\text{Ti}_3\text{O}_{12}$ phase.

Raman spectroscopy is sensitive to the fluctuation in internal crystal structure of samples. Fig. 3(a) shows the Raman peaks at 131, 156, 214, 239, 342, 405, 445, 541, 559, 610, 795 and 820 cm^{-1} correspond to the typical monoclinic layered perovskite crystalline structure [13,29]. The bands at 156, 239, 342 and 405 cm^{-1} are most likely from the La-O bond vibration. The stretching of octahedral O-Ti-O bonds can be found at 445 (E_g mode), 610 and 795 cm^{-1} . The peaks at 131 (B_{1g} mode) and 820 (B_{2g} mode) cm^{-1} are similar to the Ti-O bond stretching vibration for the 6-fold coordinated Ti in rutile TiO_2 [30,31]. The fine Raman peaks confirm the formation of monoclinic layered perovskite phase $\text{La}_2\text{Ti}_2\text{O}_7$

doped with Bi element. The Bi doping could result in crystal distortion in $\text{La}_2\text{Ti}_2\text{O}_7$ lattice and generate crystal defects. The peaks become broader and shift towards high wavenumber with the increase in Bi content.

The Raman peaks of 0.4LBTO at 315, 545 and 849 cm^{-1} correspond to the typical orthorhombic layered perovskite structure [32,33]. $\text{Bi}_4\text{Ti}_3\text{O}_{12}$ with orthorhombic crystal structure has 24 ($6A_g + 2B_{1g} + 8B_{2g} + 8B_{3g}$) Raman active vibration modes. However, less number of peaks are observed in the 0.4LBTO Raman spectrum because the La doping. The high-frequency bands originate from the various stretching and bending vibrations of TiO_6 octahedra in the perovskite [$\text{Bi}_2\text{Ti}_3\text{O}_{10}$] $^{2-}$ layers. The bands at 849, and 315 cm^{-1} can be ascribed to the A_{1g} mode, reflected from the octahedral stretching mode of O-Ti-O stretching vibration. The bands at 545, 269 and 235 cm^{-1} are from B_{2g} and B_{3g} modes. The B_{3g} mode is generally caused by TiO_6 octahedron lattice strain or partial oxygen vacancy. The peaks below 220 cm^{-1} are from the vibration of Bi and O atoms in the [Bi_2O_2] $^{2+}$ layers [20,34]. The band at 791 is a new peak after doping La ions. The peaks of 0.1BTO/LTO-OV are weaker than that of 0.1BTO/LTO as shown in Fig. 3(b), meaning the deformation of crystal structure and disorder surface damages induced by the oxygen vacancies [35,36].

Fig. 3(c) shows the FT-IR spectra of part samples. The vibration peaks at 575 and 543 cm^{-1} are characterized as Ti-O and La-O stretching vibrations, respectively [13,23,37]. The vibration peak of La-O of 0.1BTO/LTO-OV becomes weak in comparison with 0.1BTO/LTO, indicating the lattice oxygen vacancies mainly appear around La ions after heat treatment in the nitrogen atmosphere. New peaks at 1490 cm^{-1} and 723 cm^{-1} are attributed to the stretching C-O and H-O-H bonds of the species [38,39] absorbed by the surface oxygen vacancies. The solid-state ESR spectra are measured to further confirm the oxygen

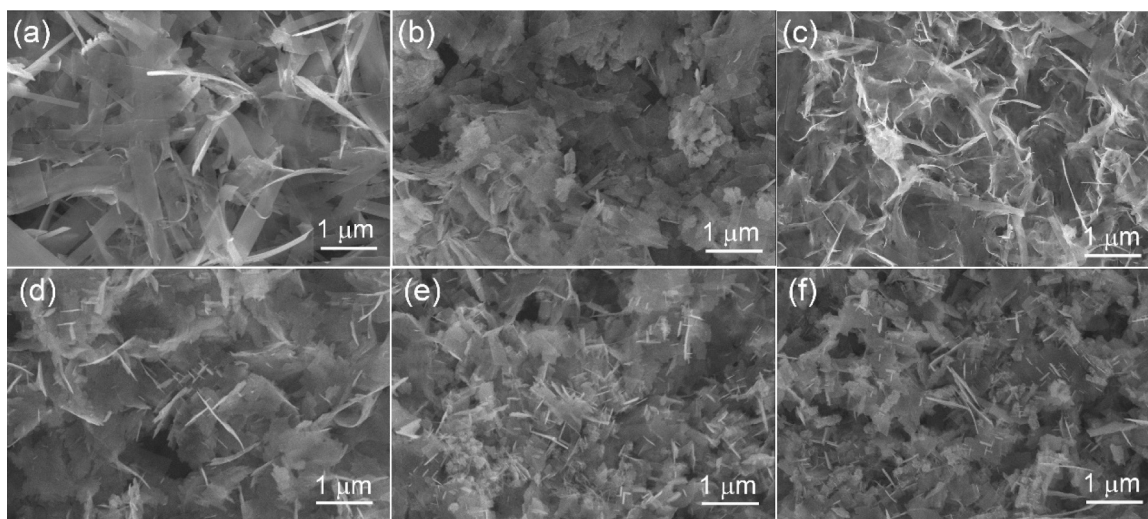


Fig. 4. SEM images of (a) pure $\text{La}_2\text{Ti}_2\text{O}_7$, (b) 0.05BTO/LTO, (c) 0.1BTO/LTO, (d) 0.2BTO/LTO, (e) 0.3BTO/LTO and (f) 0.4LBTO.

defects in samples. Fig. 3(d) shows both 0.1BTO/LTO and 0.1BTO/LTO-OV exhibit a single Lorentz line with a g-value of around 2.003 from oxygen vacancy [3,8,9,36]. However, the pure $\text{La}_2\text{Ti}_2\text{O}_7$ does not exhibit a significant oxygen vacancy characteristic peak, indicating that the oxygen defects in 0.1BTO/LTO can be attributed to the crystal distortion in $\text{La}_2\text{Ti}_2\text{O}_7$ and $\text{Bi}_4\text{Ti}_3\text{O}_{12}$ lattices induced by Bi and La doping, respectively [40,41]. The ESR signal is much enhanced in 0.1BTO/LTO-OV powders, confirming more oxygen vacancies via heat treatment in the nitrogen atmosphere.

Fig. 4 displays typical SEM images of part samples. Pure $\text{La}_2\text{Ti}_2\text{O}_7$ shows regular long ultrathin nanosheets stacked together. With the increase in Bi concentration, the samples transfer to irregular nanosheets with different sizes, which inherit the original layered structure of $\text{La}_2\text{Ti}_2\text{O}_7$. Other ultrathin nanosheets appear in the composite sample, belonging to the orthorhombic $\text{Bi}_4\text{Ti}_3\text{O}_{12}$ phase [42,43]. The uniform cross structure consists of self-assembled nanosheets. Part amorphous nanoparticles assemble into a compact cross before the crystallization. This array configuration could greatly reduce the surface energy of the nanosheets.

Fig. 5 shows TEM images of the as-prepared 0.1BTO/LTO and 0.3BTO/LTO composites. 0.1BTO/LTO powder in Fig. 5(a) has irregular nanosheets similar to the SEM images. The SAED pattern well meets the monoclinic $\text{La}_2\text{Ti}_2\text{O}_7$ with (0 2 0) and (2 0 0) crystal planes and their included angle of 90° , indicating the main $\text{La}_2\text{Ti}_2\text{O}_7$ phase in the 0.1BTO/LTO powder. But the $\text{Bi}_4\text{Ti}_3\text{O}_{12}$ phase was captured by the XRD pattern. The corresponding EDS elemental mappings show the Bi ions are evenly distributed in the sample, suggesting Bi^{3+} ions replace part La^{3+} ions in $\text{La}_2\text{Ti}_2\text{O}_7$ lattice. Fig. 5(b) clearly displays the cross structure of 0.3BTO/LTO composite. The insets show its high-resolution transmission electron microscopy (HRTEM) images and corresponding SAED patterns. There are two different SAED patterns. One is from the orthorhombic $\text{Bi}_4\text{Ti}_3\text{O}_{12}$ phase with (0 0 12) and (0 2 0) crystal planes and their included angle of 90° . Another meets the monoclinic $\text{La}_2\text{Ti}_2\text{O}_7$ structure with ($\bar{4}$ 0 1) crystal plane. The lattice fringes with d spacings of 0.277 and 0.212 nm in HRTEM are assigned to the (0 2 0) and ($\bar{2}$ 1 5) planes of $\text{La}_2\text{Ti}_2\text{O}_7$, respectively. The interplane distance of 0.297 nm well matches the (1 1 7) plane of $\text{Bi}_4\text{Ti}_3\text{O}_{12}$. The (0 2 0) plane of $\text{La}_2\text{Ti}_2\text{O}_7$ is close to the (1 1 7) plane of $\text{Bi}_4\text{Ti}_3\text{O}_{12}$, providing a foundation to form a heterojunction between $\text{La}_2\text{Ti}_2\text{O}_7$ and $\text{Bi}_4\text{Ti}_3\text{O}_{12}$. The interfacial connections with lattice crossing through two phases could serve as migration paths to facilitate charge separation and improve the synergistic effects for photocatalytic performance. The corresponding EDS elemental mappings reveal La, Bi, Ti and O are uniformly distributed throughout the nanosheet-assembled hierarchical architectures,

suggesting the uniform Bi doping in $\text{La}_2\text{Ti}_2\text{O}_7$ lattice and La doping in $\text{Bi}_4\text{Ti}_3\text{O}_{12}$ lattice.

Fig. 6(a) presents the XPS full spectra of samples. La 3d spectra in Fig. 6(b) show doublet peaks from La 3d_{3/2} and La 3d_{5/2} states with good symmetry, indicating a La^{3+} oxidation state [44,45]. The La^{3+} characteristic doublets of Bi-doped $\text{La}_2\text{Ti}_2\text{O}_7$, La-doped $\text{Bi}_4\text{Ti}_3\text{O}_{12}$ and heterojunctions positively shift to higher binding energy by ~ 0.3 eV in comparison with the pure $\text{La}_2\text{Ti}_2\text{O}_7$, meaning a loss of electrons. The symmetric peaks at 463.8 and 458.1 eV of pure $\text{La}_2\text{Ti}_2\text{O}_7$ in Fig. 6(c) are from Ti 2p_{1/2} and 2p_{3/2} states, assigned to the Ti^{4+} in TiO_6 octahedral slabs [44]. After introducing Bi ions, its binding energies shift to 464.1 and 458.4 eV, also suggesting a decrease in electron density due to the formation of O-Ti-Bi bonds [22]. The O 1s spectra of samples are fitted to three peaks at around 529.5, 531.0 eV and 532.7 eV as shown in Fig. 6(d). The peak at 529.5 eV belongs to the oxygen-metal bonds in crystal lattices [46]. The weak peaks at around 532.7 eV refer to OH^- species from the adsorbed hydroxyl groups H_2O and CO_3^{2-} [4,47]. The middle peak can be associated with oxygen in crystal lattices near the oxygen vacancies [35,48]. Clearly, this peak of 0.1BTO/LTO-OV shifts to 530.7 eV and becomes stronger, further confirming more oxygen vacancies after heat treatment in a nitrogen atmosphere. The binding energies of 164.1 and 158.8 eV in Fig. 6(e) are attributed to Bi 4f_{5/2} and 4f_{7/2}. The binding peaks of heterojunctions negatively shift to low energy in comparison with those of La-doped $\text{Bi}_4\text{Ti}_3\text{O}_{12}$ phase, indicating $\text{Bi}_4\text{Ti}_3\text{O}_{12}$ receives electrons. The change in binding energy means electrons migrate from Bi-doped $\text{La}_2\text{Ti}_2\text{O}_7$ to La-doped $\text{Bi}_4\text{Ti}_3\text{O}_{12}$ to build an electric field from $\text{Bi}_4\text{Ti}_3\text{O}_{12}$ to $\text{La}_2\text{Ti}_2\text{O}_7$ to be an S-scheme heterojunction. The peaks of 0.1BTO/LTO-OV shift to low energy due to more oxygen vacancies in the sample.

3.2. Photoelectric properties and energy band structure analysis

The optical properties of samples were characterized by UV-vis absorption spectra as shown in Fig. 7(a). The absorption edge of pure $\text{La}_2\text{Ti}_2\text{O}_7$ is at about 320 nm, indicating that $\text{La}_2\text{Ti}_2\text{O}_7$ is difficult in response to visible light. The Bi-doped $\text{La}_2\text{Ti}_2\text{O}_7$ samples show a redshift. Bi ions into $\text{La}_2\text{Ti}_2\text{O}_7$ lattice introduce metal impurity energy levels at the bottom of conduction band of $\text{La}_2\text{Ti}_2\text{O}_7$, reducing its band gap to promote light absorption [49]. 0.4LBTO exhibits a weak absorption peak in the 500 – 540 nm wavelength. The lattice will distort after part substitution of trivalent cations in the crystal lattice, resulting in surface oxygen vacancies [40]. The donor energy levels are introduced in the $\text{Bi}_4\text{Ti}_3\text{O}_{12}$ band with the oxygen vacancies, reducing its band gap and causing the weak absorption peak [50]. Similarly, there should be a peak

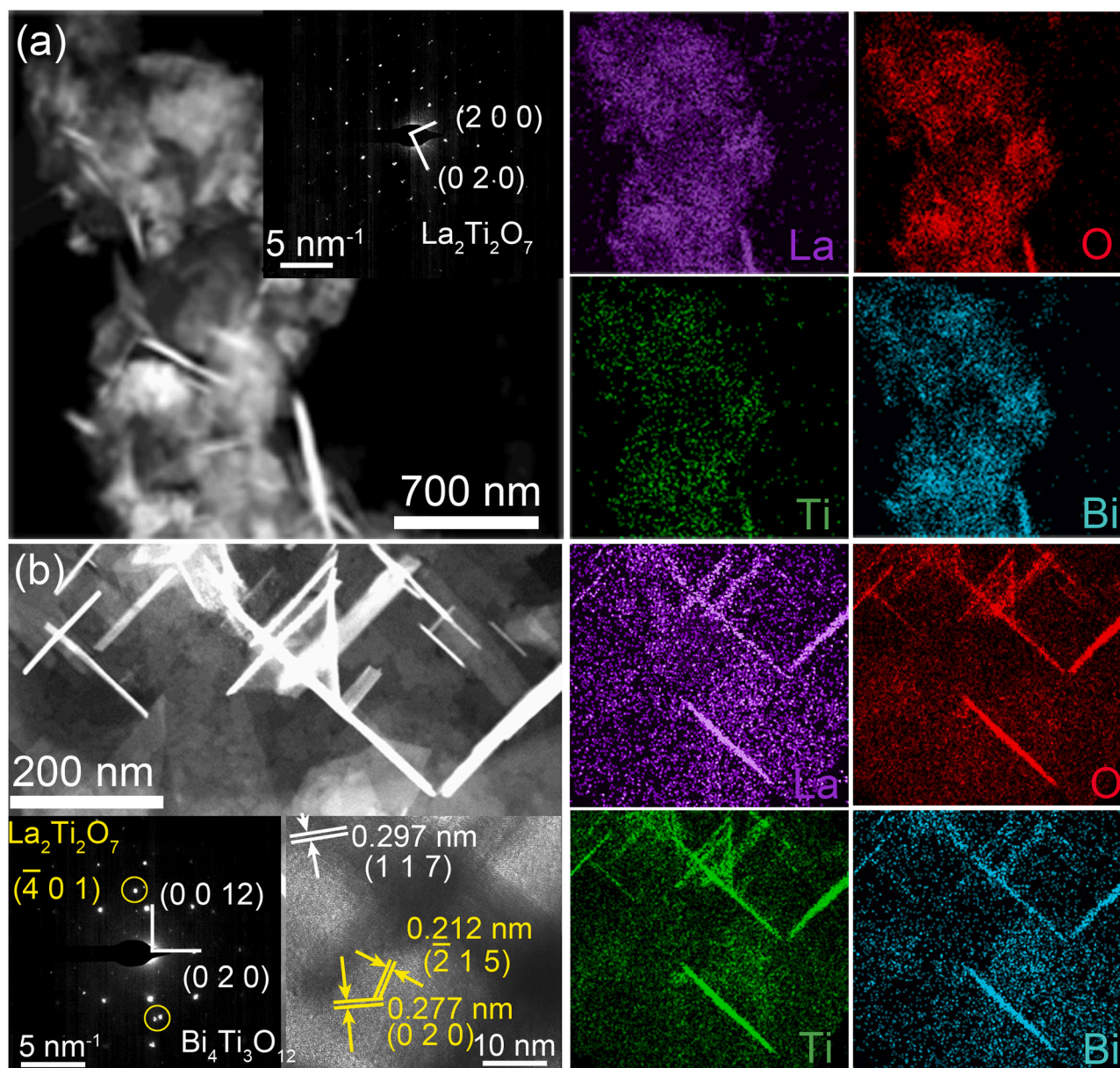


Fig. 5. TEM images of (a) 0.1BTO/LTO and (b) 0.3BTO/LTO and their EDS elemental mapping images. The insets show the corresponding SAED images and HRTEM images.

in the UV–vis absorption spectra of Bi-doped $\text{La}_2\text{Ti}_2\text{O}_7$ sample. But there is no clear peak in the spectra due to the low Bi doping content. The composite photocatalysts combine both characteristics, showing two absorption peaks, especially for 0.3BTO/LTO. 0.1BTO/LTO-OV has a further redshift and higher absorption intensity in the visible range after introducing more oxygen vacancies. The construction of oxygen vacancies into semiconductors can effectively promote their light absorption [2,51]. 0.1BTO/LTO-OV exhibits two clear absorption peaks based on 0.1BTO/LTO sample. They are caused by the oxygen vacancies that produce donor levels in the two semiconductors, which promotes the light-capturing capability [51]. The oxygen vacancies were confirmed by the ESR result as shown in Fig. 3(d).

The energy band gap of semiconductor meets the following formula.

$$\alpha h\nu = A(h\nu - E_g)^{n/2} \quad (4)$$

where α , ν , E_g and A are the absorption coefficient, light frequency, band gap energy and a constant, respectively. n depends on the mode of photon transition in semiconductors. $n = 1$ or 3 is a direct transition

semiconductor while $n = 4$ or 6 is an indirect transition semiconductor [52]. n was determined as 1 for the pure phase samples by plotting $\ln(\alpha h\nu)$ versus $\ln(h\nu - E_g)$ with the data in high slope region as shown in Fig. 7(b), meaning that both $\text{La}_2\text{Ti}_2\text{O}_7$ and $\text{Bi}_4\text{Ti}_3\text{O}_{12}$ are direct transition semiconductors. Then, the band gap E_g is determined by the intercept on the $h\nu$ axis through linearly fitting $(\alpha h\nu)^2$ versus $h\nu$ as shown in Fig. 7(c). The band gaps of $\text{La}_2\text{Ti}_2\text{O}_7$, 0.01BLTO and 0.4LBTO are 3.82, 3.58 and 3.59 eV, respectively, as shown in Table 1.

The electronic structures were simulated by GGA with PBE embedded in the VASP code for the single-phase samples as shown in Fig. 8. $\text{La}_2\text{Ti}_2\text{O}_7$, $\text{La}_7\text{BiTi}_8\text{O}_{28}$, $\text{Bi}_4\text{Ti}_3\text{O}_{12}$ and $\text{Bi}_2\text{La}_2\text{Ti}_3\text{O}_{12}$ are direct transition semiconductors, which are consistent with the experimental results. The bandgap of $\text{La}_7\text{BiTi}_8\text{O}_{28}$ is a little smaller than that of $\text{La}_2\text{Ti}_2\text{O}_7$, which is in agreement with the change between 0.01BLTO and $\text{La}_2\text{Ti}_2\text{O}_7$. But the bandgap of $\text{Bi}_2\text{La}_2\text{Ti}_3\text{O}_{12}$ becomes larger than that of $\text{Bi}_4\text{Ti}_3\text{O}_{12}$. This is caused by the difference in atomic electronic structure between $\text{La } 5d^{16}s^2$ and $\text{Bi } 6s^26p^3$. The density of states shows that the valence band maximum is primarily composed of O 2p orbit while the

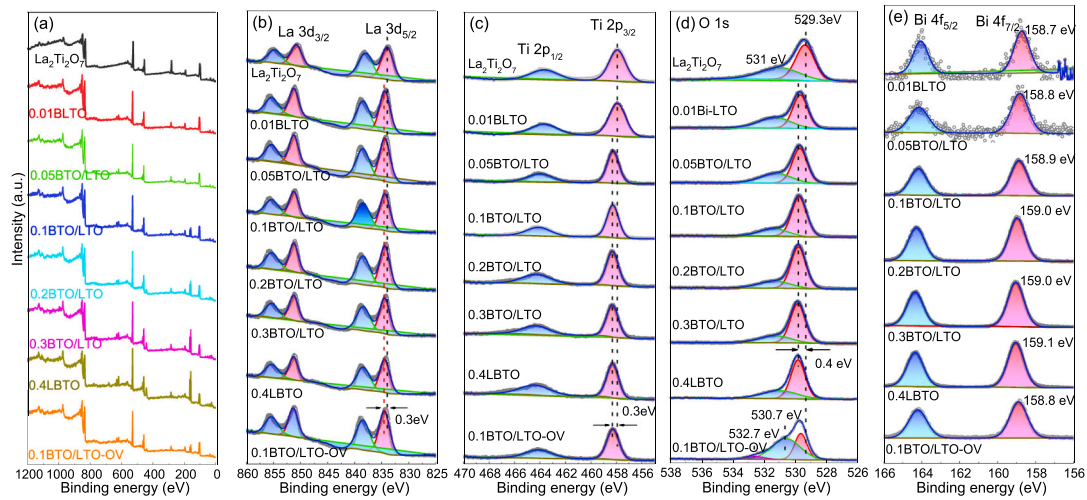


Fig. 6. XPS spectra of pure $\text{La}_2\text{Ti}_2\text{O}_7$, Bi-doped $\text{La}_2\text{Ti}_2\text{O}_7$, La-doped $\text{Bi}_4\text{Ti}_3\text{O}_{12}$ and heterojunctions. (a) Survey spectra, (b) La 3d, (c) Ti 2p, (d) O 1s and (e) Bi 4f.

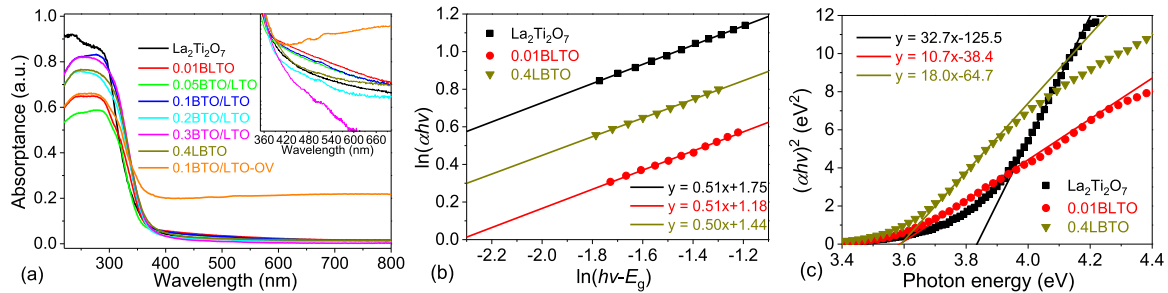


Fig. 7. (a) UV-vis absorption spectra of $\text{La}_2\text{Ti}_2\text{O}_7$, Bi-doped $\text{La}_2\text{Ti}_2\text{O}_7$, La-doped $\text{Bi}_4\text{Ti}_3\text{O}_{12}$ and heterojunctions, where the enlarged spectra show the absorption peaks. (b) Linear relationship between $\ln(h\nu - E_g)$ and $\ln(ah\nu)$ of the single-phase samples to determine the semiconductor type, and (c) relationship between $(ah\nu)^2$ and photon energy to calculate the band gaps.

Table 1

Band parameters and carrier concentration of pure $\text{La}_2\text{Ti}_2\text{O}_7$, Bi-doped $\text{La}_2\text{Ti}_2\text{O}_7$ and La-doped $\text{Bi}_4\text{Ti}_3\text{O}_{12}$.

Samples	Band gap E_g (eV)	Fermi level E_F (eV)	Conduction band E_c (eV)	Valence band E_v (eV)	Carrier concentration N_D (cm^{-3})
$\text{La}_2\text{Ti}_2\text{O}_7$	3.82	-0.453	-0.52	3.27	4.31×10^{20}
0.01BLTO	3.58	-0.578	-0.66	3.01	6.23×10^{20}
0.4LBTO	3.59	-0.373	-0.45	3.14	5.47×10^{20}

conduction band minimum is mainly occupied by Ti 3d orbit.

Fig. 9 shows the Mott-Schottky measurements of single-phase samples to elucidate the flat-band potential (V_{fb}) and carrier concentration (N_D) of semiconductors [53], which satisfy the relationship

$$\frac{1}{C^2} = \frac{2}{\epsilon\epsilon_0 e N_D} \left(V - V_{fb} - \frac{k_B T}{e} \right) \quad (5)$$

where C is the semiconductor capacitance per square centimeter, V is the applied voltage, T is the absolute temperature, e is the electronic charge, k_B , ϵ_0 and ϵ are the Boltzmann's constant, permittivity in a vacuum and relative permittivity of semiconductor, respectively. Therefore, plots of $1/C^2$ against V should yield a straight line, by which N_D can be conveniently found from the slope. The Fermi energy (E_F) is nearly flat-band potential, which is the intercept of the x-axis. The bottom energy of conduction band E_C and Fermi level E_F in n -type non-degenerate semiconductors obey

$$E_C = E_F + k_B T \ln \frac{N_C}{n_0}, N_C = 2 \left(\frac{m_n^* k_B T}{2\pi \hbar^2} \right)^{3/2} \quad (6)$$

where N_C is the effective state density of the conduction band, m_n^* is the effective mass of electrons at the bottom of conduction band (E_C), and \hbar is the reduced Planck constant. Then, we obtain the band parameters as shown in Table 1. The carrier concentration increases after doping the foreign elements, caused by the oxygen vacancies. The measured potentials versus Ag/AgCl electrode can be converted to the normal hydrogen electrode (NHE) potentials using the Nernst equation [40,54]. The conduction band E_C of 0.01BLTO increases to -0.66 V (vs. NHE) after doping Bi ions, enjoying stronger exchange-reduction ability. Then, the electrons in the conduction band of 0.01BLTO can directly react with $\text{O}_2/\bullet\text{O}_2^-$ (-0.33 eV vs. NHE). The valence band of 0.4LBTO is +3.14 eV, which is more positive than both +1.99 eV vs. NHE for $\text{OH}^-/\bullet\text{OH}$ and 2.37 eV vs. NHE for $\text{H}_2\text{O}/\bullet\text{OH}$. Then, the holes in the 0.4LBTO valence band can directly react with H_2O to H^+ and active $\bullet\text{OH}$ [55].

3.3. Photocatalytic performances

The photocatalytic activities of as-prepared samples were evaluated by photocatalytic NO removal experiments. Fig. 10(a) shows NO can be quickly purified and the removal ratios reach equilibrium in 8 min. The NO removal ratio of pristine $\text{La}_2\text{Ti}_2\text{O}_7$, 0.01BLTO and 0.4LBTO is 23%, 36% and 42% in 8 min, respectively, suggesting photocatalytic performance is improved in the doped samples. The photocatalytic ability of heterojunctions is further enhanced. Among them, 0.1BTO/LTO sample

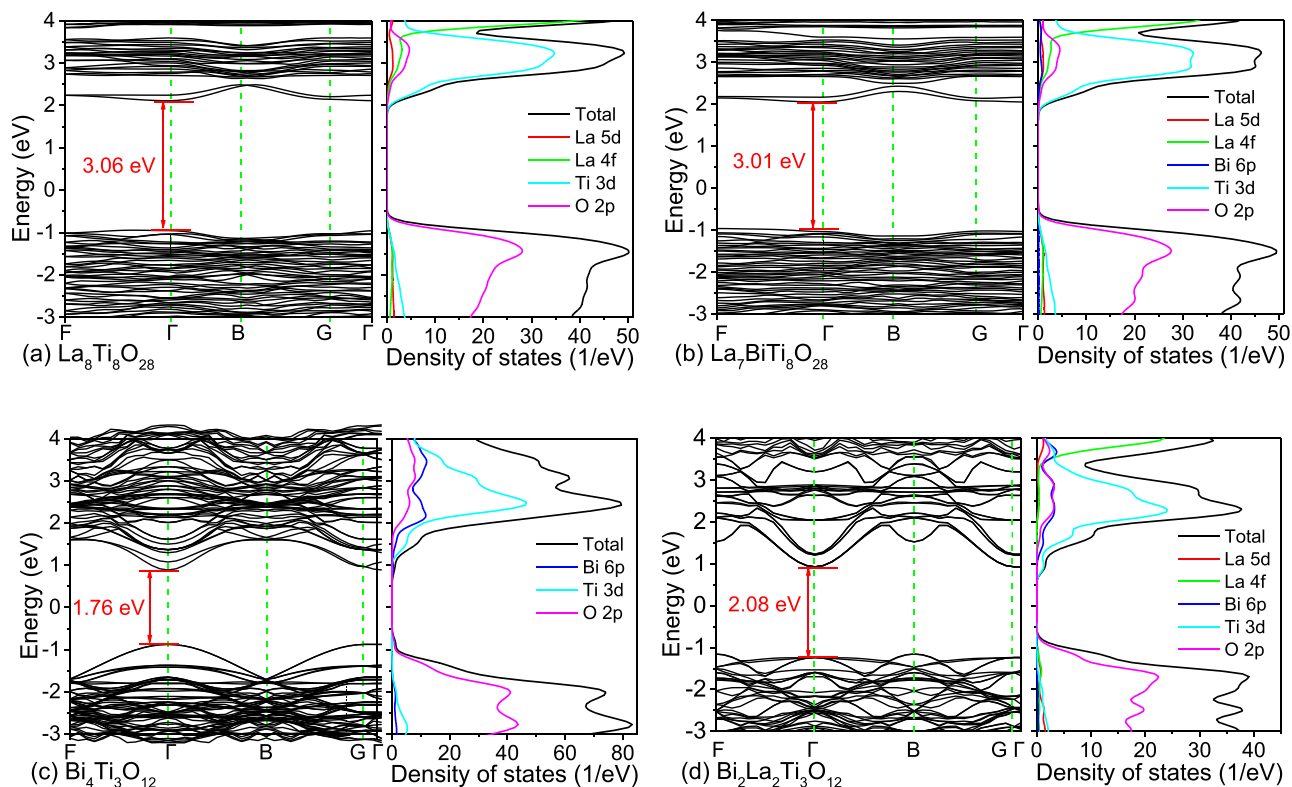


Fig. 8. Calculated band structure and density of states of (a) $\text{La}_2\text{Ti}_2\text{O}_7$, (b) $\text{La}_7\text{BiTi}_8\text{O}_{28}$, (c) $\text{Bi}_4\text{Ti}_3\text{O}_{12}$ and (d) $\text{Bi}_2\text{La}_2\text{Ti}_3\text{O}_{12}$, corresponding to the pure phases.

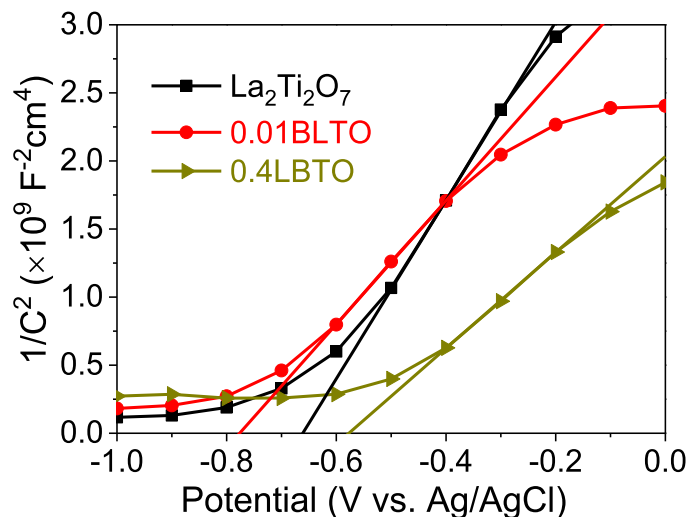


Fig. 9. Mott-Schottky plot of $\text{La}_2\text{Ti}_2\text{O}_7$, Bi-doped $\text{La}_2\text{Ti}_2\text{O}_7$ and La-doped $\text{Bi}_4\text{Ti}_3\text{O}_{12}$.

enjoys the highest NO removal ratio of 48%. This is mainly attributed to the internal electric field at the interface between Bi-doped $\text{La}_2\text{Ti}_2\text{O}_7$ and La-doped $\text{Bi}_4\text{Ti}_3\text{O}_{12}$, which facilitates the separation of photogenerated electron-hole pairs and allows more carriers to migrate to the sample surface to participate in the removal of NO gas [7]. The NO removal ratio is further improved to 55% by 0.1BTO/LTO-OV, ascribed to the more oxygen vacancies in sample after the heat treatment. The introduction of oxygen vacancy can effectively improve the charge transfer rate and electron-hole separation efficiency and provide more active sites to enhance the adsorption and reaction ability of pollutants [56]. Usually, the oxygen vacancies include two types, i.e., V_O' (trapped one

electron) and V_O'' (trapped two electrons). Following the interfacial two-electron charging ($\text{V}_\text{O}'' + \text{O}_2 \rightarrow \text{V}_\text{O}-\text{O}_2^{\cdot-}$) and subsequent one-electron back-donation ($\text{V}_\text{O}-\text{O}_2^{\cdot-} + \text{NO} \rightarrow \text{V}_\text{O}-\text{NO}_3^- + \text{e}^-$) process, the back-donated electron could be retrapped by V_O to produce a new single-electron-trapped V_O' , simultaneously triggering a second round of NO oxidation ($\text{V}_\text{O}' + \text{O}_2 \rightarrow \text{V}_\text{O}-\text{O}_2^{\cdot-}$) [10]. Therefore, constructing the oxygen vacancies on the 0.1BTO/LTO-OV surface is necessary and has a significant effect on enhancing the photocatalytic performance in photo-oxidative NO removal.

The intermediate product NO_2 during the photo-oxidation is a notorious member in NO_x with even more toxicity and hazardous than

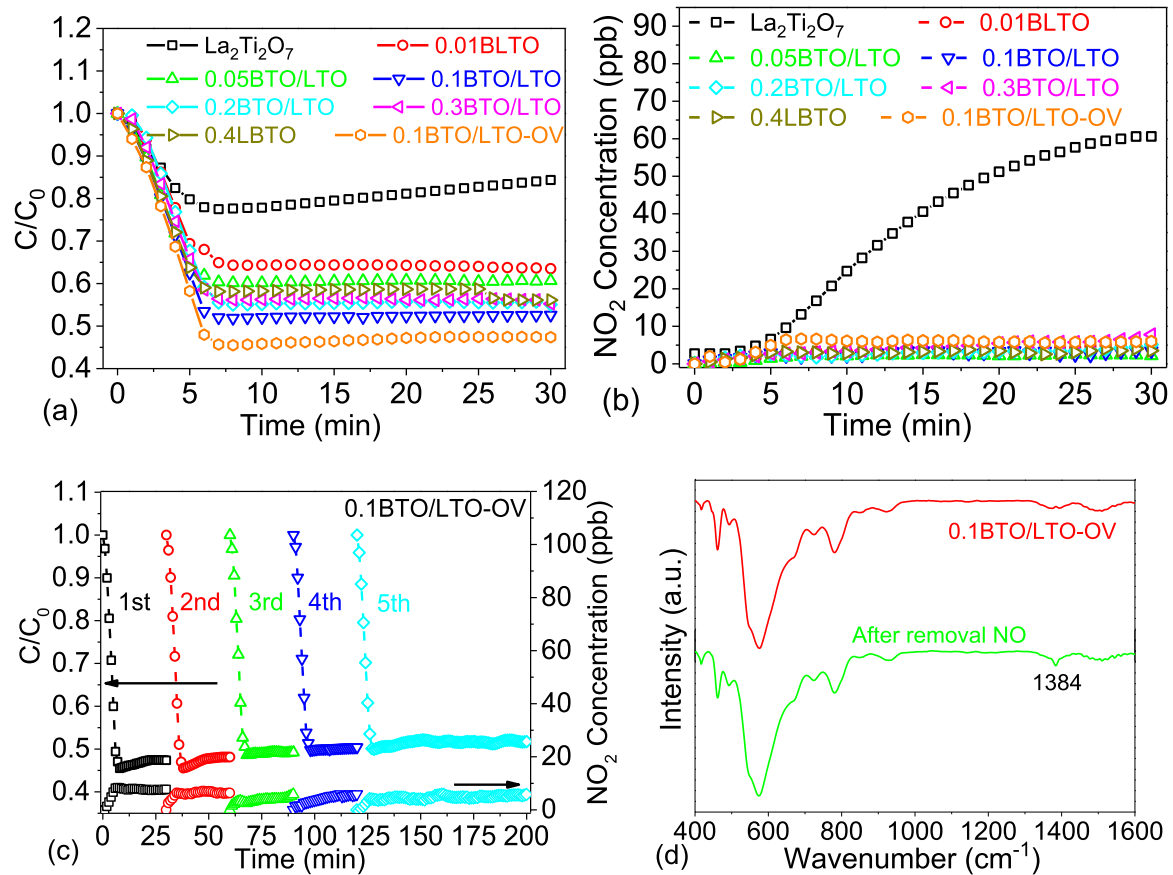


Fig. 10. (a) Photocatalytic NO removal and (b) NO₂ production of pure La₂Ti₂O₇, Bi-doped La₂Ti₂O₇, La-doped Bi₄Ti₃O₁₂ and heterojunctions. (c) Photocatalytic stability of NO removal and NO₂ generation over 0.1BTO/LTO-OV in cyclic tests and (d) FT-IR spectra of 0.1BTO/LTO-OV before and after five photocatalytic NO runs.

Table 2

Comparison of removal performance of NO gas by various photocatalysts.

Photocatalyst	NO source (ppb)	C ₀ /C	NO ₂ generation (ppb)	Light resource	Active species/target products	Year, ref.
ZnWO ₄	400	0.4	N/A	300 W Xenon lamp	•OH and •O ₂ ⁻ /NO ₃ ⁻	2016 [64]
(BiO) ₂ CO ₃	430	0.53	15.6	Visible light	•O ₂ ⁻ and •OH/mo-NO ₃ ⁻ and bi-NO ₃ ⁻	2021 [65]
Vo-BiOCl	500	0.6	80	Xenon lamp	•O ₂ ⁻ /NO ₂ and NO ₃ ⁻	2019 [10]
Vo-Bi ₂ MoO ₆ Nanosheets	600	0.47	90	Visible light	e ⁻ , ¹ O ₂ and •O ₂ ⁻ /NO ₂ and NO ₃ ⁻	2022[2]
Bi/BiOBr nanoflowers	800	0.63	29	300 W Xenon lamp	e ⁻ , h ⁺ and •O ₂ ⁻ /NO ₂ and NO ₃ ⁻	2023 [60]
Bi ₁₂ GeO ₂₀ /Bi ₂ S ₃	580	0.46	8	500 W Xenon lamp	e ⁻ , h ⁺ and •O ₂ ⁻ /NO ₃ ⁻	2022[8]
g-C ₃ N ₄	600	0.57	50	Visible light	h ⁺ and e ⁻ /NO ₃ ⁻	2022 [66]
g-C ₃ N ₄ microtubes	400	0.33	25	Visible light	•O ₂ ⁻ and h ⁺ /NO ₃ ⁻	2019 [67]
Pd/g-C ₃ N ₄	600	0.75	60	Visible light	h ⁺ , •O ₂ ⁻ and •OH/NO ₃ ⁻	2022 [68]
CaCO ₃ /g-C ₃ N ₄	550	0.51	120	Visible light	¹ O ₂ , •OH and •O ₂ ⁻ /NO ₂ and NO ₃ ⁻	2023 [61]
g-C ₃ N ₄ /TiO ₂ -Ti ₃ C ₂	500	0.61	35	300 W Xenon lamp	e ⁻ , •O ₂ ⁻ and •OH/NO ₃ ⁻	2021 [69]
3D-2D Bi ₄ O ₅ Br ₂ -GO	550	0.54	20	Visible light	e ⁻ and •O ₂ ⁻ /NO ₃ ⁻	2021 [70]
Bi ₂ Ti ₂ O ₇ /CaTiO ₃	600	0.77	70	Visible light	•O ₂ ⁻ /NO ₃ ⁻	2022[3]
TiO ₂ -s/Carbon	430	0.55	13	Visible light	•O ₂ ⁻ and •OH/NO ₃ ⁻	2021 [71]
BiOBr/BiOI	600	0.57	50	Visible light	h ⁺ , •O ₂ ⁻ and ¹ O ₂ /NO ₃ ⁻	2019 [72]
Bi-doped La ₂ Ti ₂ O ₇ /La-doped Bi ₄ Ti ₃ O ₁₂ S-scheme heterojunction	430	0.52	5.6	300 W Xenon lamp	e ⁻ , ¹ O ₂ , h ⁺ , •O ₂ ⁻ and •OH/NO ₃ ⁻	This work

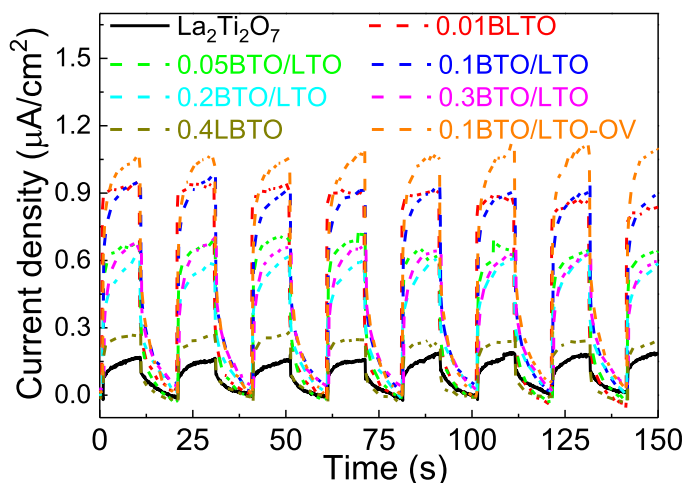


Fig. 11. (a) Photocurrents of the pure $\text{La}_2\text{Ti}_2\text{O}_7$, Bi-doped $\text{La}_2\text{Ti}_2\text{O}_7$, La-doped $\text{Bi}_4\text{Ti}_3\text{O}_{12}$ and heterojunctions.

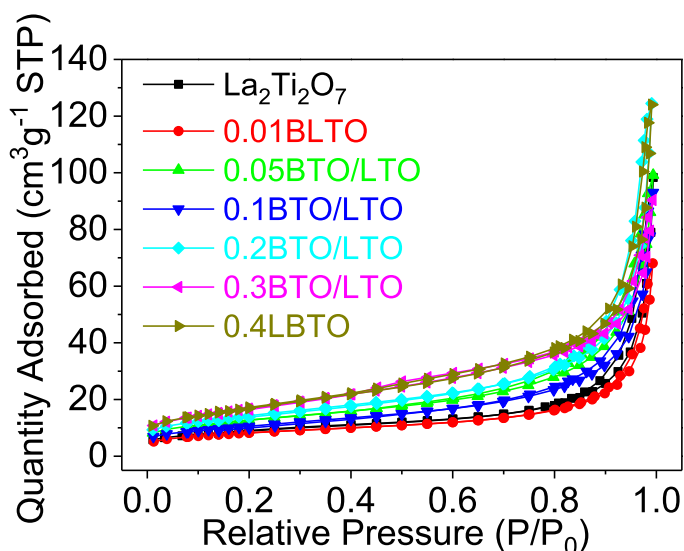


Fig. 12. Nitrogen adsorption-desorption curves for the pure $\text{La}_2\text{Ti}_2\text{O}_7$, Bi-doped $\text{La}_2\text{Ti}_2\text{O}_7$, La-doped $\text{Bi}_4\text{Ti}_3\text{O}_{12}$ and heterojunctions at 77 K.

the NO gas [2,3]. NO_2 production was also monitored during the NO removal reaction as shown in Fig. 10(b). The NO_2 yields of xBTO/LTO are much lower than that of pure $\text{La}_2\text{Ti}_2\text{O}_7$ (60 ppb) and the 0.1BTO/LTO enjoys the lowest NO_2 production of only 3.4 ppb. The NO_2 concentration of 0.1BTO/LTO-OV was still kept low level to avoid the second pollutant. The oxygen vacancies-modified S-scheme heterojunction of Bi-doped $\text{La}_2\text{Ti}_2\text{O}_7$ and La-doped $\text{Bi}_4\text{Ti}_3\text{O}_{12}$ shows greatly improved photocatalytic performance, especially in the inhibition of NO_2 secondary pollutant, in comparison with the recent reports as shown in Table 2.

The cycling experiment was performed to further explore the catalyst stability. Five successive runs of catalytic NO removal are conducted under identical conditions. The sample 0.1BTO/LTO-OV exhibits good durability, maintaining 95% of the catalytic activity in the first run after five cycles of testing with less NO_2 production than 10 ppb as shown in Fig. 10(c). The little reduction of catalytic performance is attributed to the accumulation of intermediates covering active sites on the surface. BTO/LTO composite exhibits excellent photocatalytic stability in removing NO. Especially, it is more environmentally friendly without generating dangerous secondary NO_2 pollution.

The FT-IR spectra of 0.1BTO/LTO-OV are tested to confirm the

Table 3

BET surface area, pore volume and average pore diameter of the samples.

Samples	Surface area ($\text{m}^2 \text{g}^{-1}$)	Pore volume ($\text{cm}^3 \text{g}^{-1}$)	Average pore diameter (nm)
$\text{La}_2\text{Ti}_2\text{O}_7$	31.94	0.152	21.51
0.01BLTO	29.05	0.101	19.76
0.05BTO/LTO	45.19	0.148	13.42
0.1BTO/LTO	47.81	0.141	15.13
0.2BTO/LTO	51.06	0.187	16.04
0.3BTO/LTO	60.695	0.134	10.43
0.4LBTO	60.96	0.187	14.38

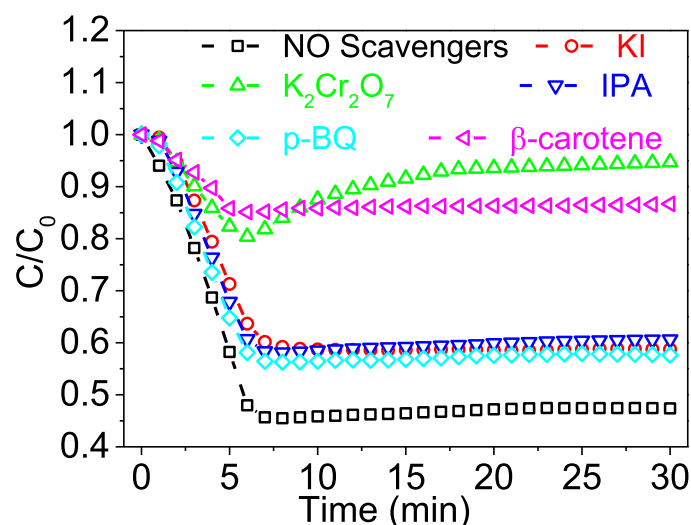


Fig. 13. Photocatalytic performance with different trapping agents over 0.1BTO/LTO-OV.

photocatalytic stability as shown in Fig. 10(d). The 0.1BTO/LTO-OV possesses all bands before and after NO removal, indicating good chemical structure stability. Two curves present the typical structure of perovskite in the range of $500 - 800 \text{ cm}^{-1}$. NO_3^- is evidenced by the little sharp peak at 1384 cm^{-1} , corresponding to NO_3^- on the sample surface after the NO photodegradation reaction [57].

3.4. Photodegradation mechanism

The photocurrent intensity of all samples instantly increases with the light excitation to high points in a short time as shown in Fig. 11. Then, it decreases rapidly to a low current with the light off to form a stable dark current. The Bi-doped $\text{La}_2\text{Ti}_2\text{O}_7$ shows a much higher photocurrent response than the pure $\text{La}_2\text{Ti}_2\text{O}_7$ sample, implying its more photo-generated carriers. La-doped $\text{Bi}_4\text{Ti}_3\text{O}_{12}$ has a similar photocurrent response with the pure $\text{La}_2\text{Ti}_2\text{O}_7$. The composite photocatalysts also exhibit higher photocurrent response via the formation of heterojunction. Its photocurrent of 0.1BTO/LTO-OV further increases in comparison with the 0.1BTO/LTO. The enhanced photocurrent is related to the oxygen vacancies, which act as electron traps to promote charge separation efficiency [2]. Therefore, the oxygen vacancies effectively suppress the backflow of electrons and holes, to achieve better electron-hole separation efficiency [36].

Fig. 12 shows the N_2 adsorption-desorption isotherm. The catalysts display type IV isotherms with hysteresis loops, indicating the existence of mesopores. 0.01BLTO shares similar specific surface area, pore volume and average pore diameter with $\text{La}_2\text{Ti}_2\text{O}_7$ as shown in Table 3. 0.4LBTO exhibits a higher surface area for its cross structure. Then, the composite photocatalysts enjoy high specific surface areas after constructing the heterojunction. The specific surface areas and porosities of

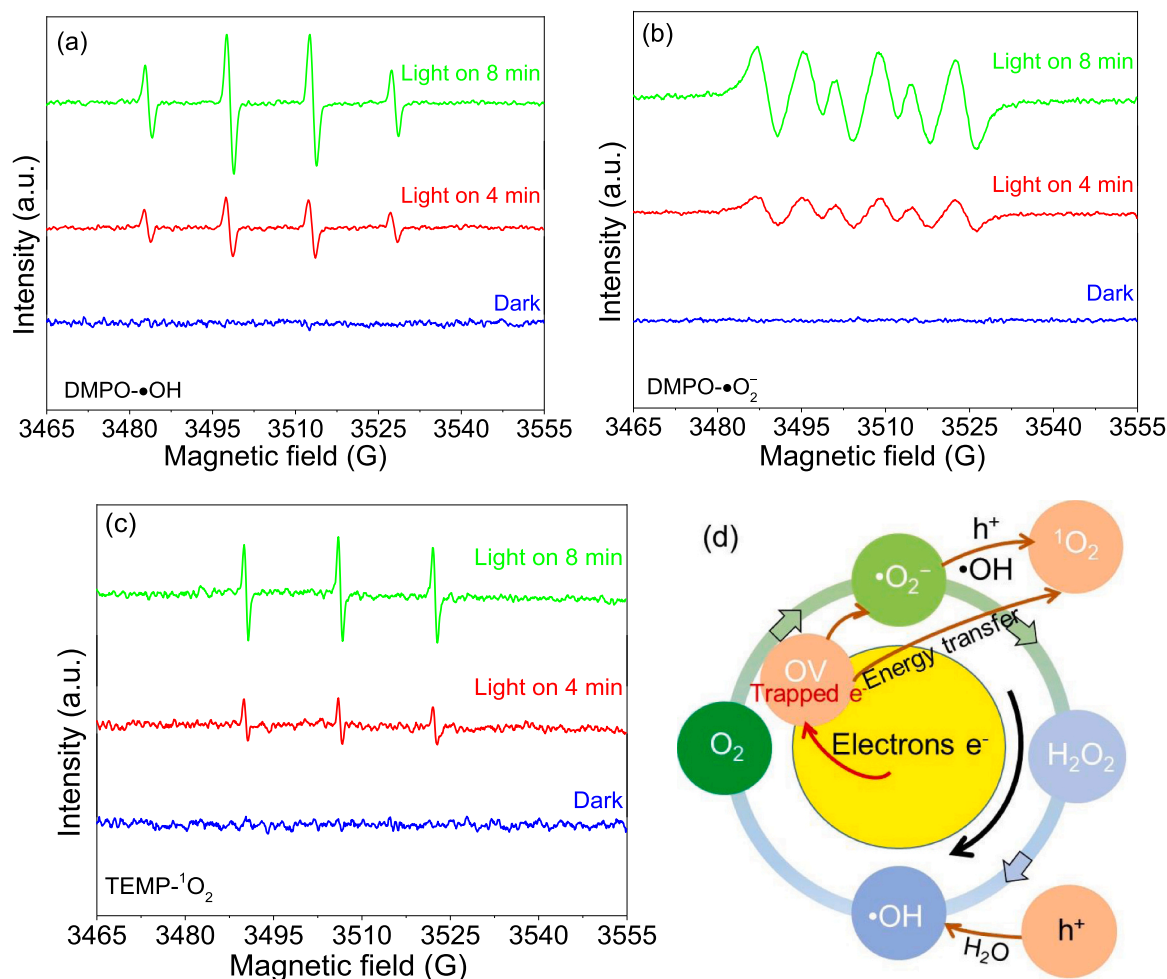


Fig. 14. ESR signals of 0.1BTO/LTO-OV for (a) $\bullet\text{OH}$, (b) $\bullet\text{O}_2^-$ and (c) $^1\text{O}_2$ in the dark and under light irradiation, and (d) schematic generation of reactive oxygen species.

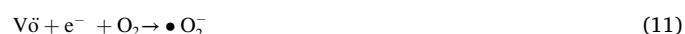
catalyst particles play important roles in the catalytic activity. Thus, the increments in specific surface area and porosity of the composite catalysts provide more active sites for pollutant degradation.

The trapping experiments were performed with different sacrificial agents to probe the mechanism of NO removal by 0.1BTO/LTO-OV. Potassium iodide (KI), potassium dichromate ($\text{K}_2\text{Cr}_2\text{O}_7$), isopropyl alcohol (IPA), p-benzoquinone (p-BQ) and β -carotene were used to trap the holes (h^+), electrons (e^-), hydroxyl radical ($\bullet\text{OH}$), superoxide radical ($\bullet\text{O}_2^-$) and singlet oxygen ($^1\text{O}_2$), respectively [2,3]. When the scavengers of e^- and $^1\text{O}_2$ are added, the photocatalytic NO removal drastically decreases as shown in Fig. 13, indicating the critical role of electrons and $^1\text{O}_2$ in the photocatalytic reactions. When the scavengers of h^+ , $\bullet\text{OH}$ and $\bullet\text{O}_2^-$ are added, the photocatalytic NO removal decreases less in the photocatalytic performance of 0.1BTO/LTO-OV, which means an involvement of h^+ , $\bullet\text{OH}$ and $\bullet\text{O}_2^-$ radicals.

ESR test is the most direct evidence to identify the radicals, such as hydroxyl radical ($\bullet\text{OH}$), superoxide radical ($\bullet\text{O}_2^-$) and singlet oxygen ($^1\text{O}_2$). The radical signal is almost undetectable in the dark as shown in Fig. 14(a)–14(c). However, typical quadruplet peaks of DMPO superoxide and hydroxyl adducts, i.e., $\text{DMPO}\cdot\text{O}_2^-$ and $\text{DMPO}\cdot\text{OH}$ are detected under illumination. In the presence of TEMP, the triplet spectra can be found for $\text{TEMP}\cdot^1\text{O}_2$, which is consistent with the results of capturing experiment. The radical signals become stronger with the illumination time, indicating more active radicals on the sample surface to promote the photocatalytic reaction.

The generation of reactive oxygen species is schematized in Fig. 14 (d) based on the above results. The abundant electrons on conduction

band or trapped by oxygen vacancies react with O_2 to form $\bullet\text{O}_2^-$ [Eqs. (7) and (11)], and then part $\bullet\text{O}_2^-$ combines with electrons to generate $\bullet\text{OH}$ with H_2O_2 as intermediates [Eqs. (8) and (9)]. The $\bullet\text{OH}$ can also be formed by hole oxidation of water [Eq. (10)]. Subsequently, part $\bullet\text{O}_2^-$ further reacts with h^+ or $\bullet\text{OH}$ to form $^1\text{O}_2$ [Eq. (12)–(14)]. At the same time, the oxygen vacancies introduce an impurity level below the conduction band, which can accommodate electrons relaxed from the conduction band. Besides, the photosensitivity of catalyst is greatly enhanced and the energy barrier of $^1\text{O}_2$ generation reduces [58]. The generation pathways of reactive oxygen species are as follows:



In situ DRIFTS spectra were measured to provide a further

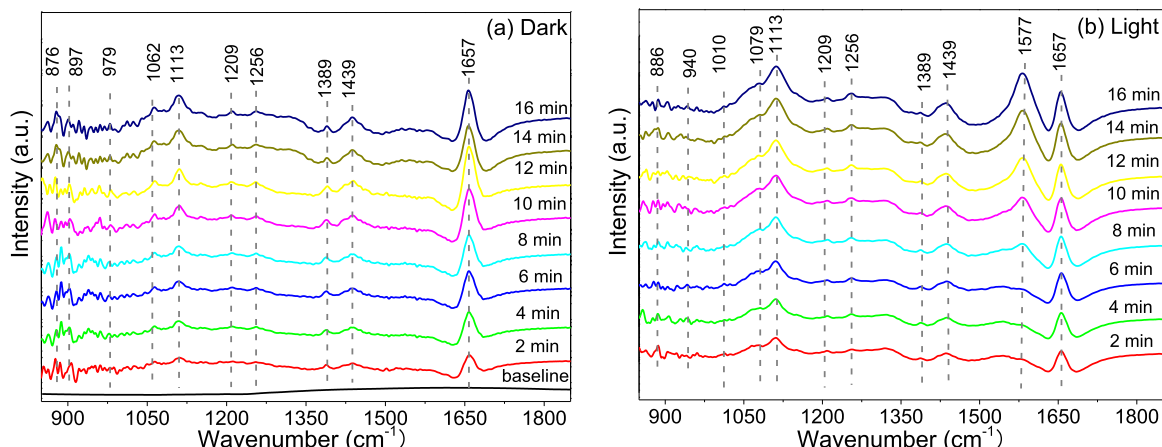


Fig. 15. In situ DRIFT spectra over 0.1BTO/LTO-OV (a) in the dark and (b) under light illumination.

Table 4

Assignments of the infrared bands observed during the photocatalytic NO oxidation processes over 0.1BTO/LTO-OV.

Wavenumbers (cm ⁻¹)	Assignment	References
886	O-O band stretching vibration	[2]
876, 979, 1062	NO ₂	[9,59,61]
897, 940	N ₂ O ₄ , N ₂ O ₄ ²⁻	[9,59]
1113	NO ⁻	[61]
1079	Chelated nitrites NO ₂ ⁻	[73]
1389	Bridge nitrites NO ₂ ⁻	[8,59]
1439	Linear nitrites NO ₂ ⁻	[9]
1256	Monodentate nitrates NO ₃ ⁻	[2,74,75]
1209	Bidentate nitrates NO ₃ ⁻	[73]
1010, 1577	Bridging nitrates NO ₃ ⁻	[60,76]
1657	NO	[5,60]

mechanistic description of the NO photocatalytic oxidation over 0.1BTO/LTO-OV. Fig. 15(a) exhibits the time-dependent characteristic peaks of NO and intermediates in the adsorption process in the dark. The bands at 1657 cm⁻¹ (NO adsorption) were detected upon exposure to NO and O₂ [5,9,59–61]. The generation of NO₂ is associated with direct

NO oxidation by O₂ (2NO + O₂ = 2NO₂ and 2NO₂ → N₂O₄), which is from a series of infrared peaks assigned to NO₂ (876, 979 and 1062 cm⁻¹) and N₂O₄ (897 cm⁻¹). Furthermore, the appearance of peaks at 1113 cm⁻¹ (NO⁻), 1389 and 1439 cm⁻¹ (NO₂⁻) was detected as middle products. Some other weak characteristics at 1209, 1256 and 1439 cm⁻¹ are considered as NO₃⁻ on the surface of 0.1BTO/LTO-OV.

Fig. 15(b) shows the in situ DRIFTS spectra associated with NO photocatalytic removal after light illumination. The peak centered at 886 cm⁻¹ is assigned to the O-O band stretching vibration of surface peroxide species, such as •O₂⁻ and ¹O₂ [2]. The infrared bands of NO₂ (876, 979, 1062 cm⁻¹) disappear after irradiating several minutes in comparison with the spectra in the dark. At the same time, a considerable number of nitrite species (NO₂⁻ and N₂O₄²⁻) appear at 1079, 1389 cm⁻¹ and 940 cm⁻¹. Particularly, new peaks at 1010 and 1577 cm⁻¹ are assigned to the bridging nitrates, which are more stable than the monodentate nitrates [60]. These peaks grow increasingly with the irradiation time, indicating that NO₂ has been further deeply oxidized to nitrate and nitrite species. Table 4 lists the main infrared bands of the adsorbed species as well as their chemical designations.

Based on the trapping experiment and in situ DRIFTS, NO captures

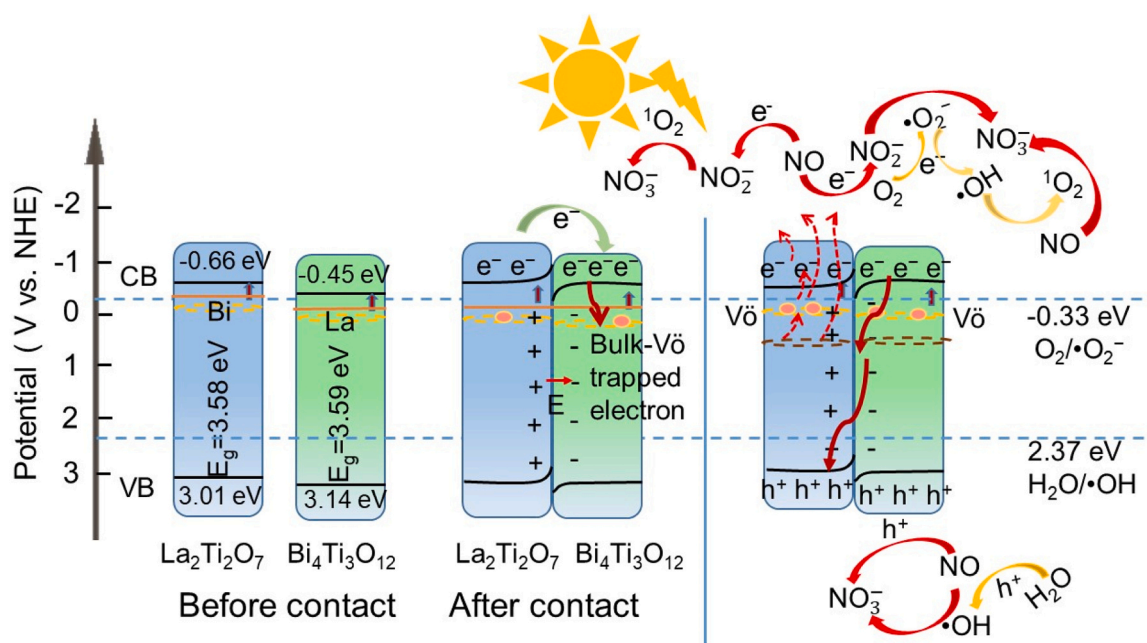


Fig. 16. Schematic illustration of charge transfers and radical generation over 0.1BTO/LTO-OV S-scheme heterojunction for the NO removal by different routes.

an electron and O_2 to trigger the transformation of surface NO_2^- and $N_2O_4^{2-}$, which helps NO further convert into NO_3^- to inhibit the intermediate NO_2 product. On the other hand, the abundant electrons in conduction band and the electrons released by oxygen vacancies can help the catalyst surface produce more 1O_2 , $\bullet O_2^-$ and $\bullet OH$ to remove the NO gas. Especially, 1O_2 owns electrophilicity and tends to oxidate the NO_2^- to NO_3^- . Based on the above analyses, the pathways of photocatalytic NO oxidation are below:

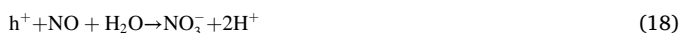
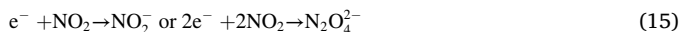


Fig. 16 illustrates the schematic of electron charge transfer and radical generation over the 0.1BTO/LTO-OV S-scheme heterojunction for NO removal by different routes. The Fermi level of Bi-doped $La_2Ti_2O_7$ is higher than that of La-doped $Bi_4Ti_3O_{12}$. After the two phases are in contact, electrons transfer from the $La_2Ti_2O_7$ conduction band to the $Bi_4Ti_3O_{12}$ conduction band until the Fermi levels reach equilibrium to form a built-in electron field from $La_2Ti_2O_7$ to $Bi_4Ti_3O_{12}$.

Under light irradiation, the photogenerated electrons are excited from the valence band of $La_2Ti_2O_7$ and $Bi_4Ti_3O_{12}$ to their conduction bands, leaving holes in their valence bands. The photogenerated electrons in space charge region of $Bi_4Ti_3O_{12}$ transfer to the interface under the built-in electric field to combine with the photogenerated holes from $La_2Ti_2O_7$ driven by the built-in electric field. Then, holes remain in the valence band of $Bi_4Ti_3O_{12}$ to keep a strong oxidation ability while the electrons remain in the conduction band of $La_2Ti_2O_7$ to keep a high reduction ability. This process achieves the spatial separation of photogenerated electrons and holes performing as an S-scheme heterojunction. At the same time, the foreign Bi^{3+} , La^{3+} and oxygen vacancies supply the energy levels to help the separation of holes and electrons.

NO easily reacts with O_2 to NO_2 , which captures e^- to be NO_2^- and $N_2O_4^{2-}$ [Reaction (15)]. This is beneficial for the conversion of NO_2 to NO_3^- , thereby inhibiting the NO_2 intermediate. The abundant electrons photogenerated on the conduction band and released from oxygen vacancies can generate more 1O_2 , $\bullet O_2^-$ and $\bullet OH$ on the catalyst surface to remove NO gas [Reactions (16), (17) and (20)]. Especially, electrophilic 1O_2 easily oxidize NO_2^- to NO_3^- . The photogenerated holes on $Bi_4Ti_3O_{12}$ valence band potential in the S-scheme heterojunction have strong oxidability for NO to NO_3^- [Reaction (18)]. The oxygen vacancy on 0.1BTO/LTO-OV surface receives electrons from inside, which has a better adsorption effect on gas and provides more active sites for photocatalytic reaction. At the same time, oxygen vacancies also directly oxidize NO to NO_3^- [Reaction (19)] [62,63].

4. Conclusions

We have successfully fabricated S-scheme heterojunctions of Bi-doped $La_2Ti_2O_7$ and La-doped $Bi_4Ti_3O_{12}$ via a simple hydrothermal method. With the increase in Bi concentration, the content of orthorhombic La-doped $Bi_4Ti_3O_{12}$ increases and the monoclinic Bi-doped $La_2Ti_2O_7$ transfers to the orthorhombic La-doped $Bi_4Ti_3O_{12}$. The 0.1BTO/LTO composite has a higher NO removal ratio (46%) and much lower NO_2 generation (only 3.4 ppb) in comparison with pristine $La_2Ti_2O_7$. The doped electronic states and oxygen defect states narrow the band gap to extend the light absorption range. The S-scheme heterojunction formed between Bi-doped $La_2Ti_2O_7$ and La-doped $Bi_4Ti_3O_{12}$ enhances the separation efficiency of photogenerated charge carriers

and improves the transfer rate of electrons across the interface. After heat treatment in N_2 environment, the enriched oxygen vacancies in heterojunction further enhance the light absorption and suppress the carrier recombination. The NO removal ratio of 0.1BTO/LTO-OV reaches 52% with only 5.6 ppb NO_2 generation. The present work provides a synergistic strategy to improve photocatalytic NO removal with doping element, building S-scheme heterojunction and introducing oxygen vacancies.

CRedit authorship contribution statement

Li Lv: Experimental investigation, Formal analysis, Writing – original draft, Visualization. **Lin Lei:** Part experimental measurements. **Qi-Wen Chen:** Part experimental research. **Cheng-Li Yin:** Theoretical research and Visualization. **Huiqing Fan:** Conceptualization, Supervision. **Jian-Ping Zhou:** Project administration, Supervision, Writing – review and editing.

Declaration of Competing Interest

We declare that we have not financial and personal relationships with other people or organizations that can inappropriately influence our work, there is no professional or other personal interest of any nature of kink in any product, service and company that could be construed as influencing the position presented in the manuscript entitled.

Data availability

No data was used for the research described in the article.

Acknowledgments

The SEM and TEM works were finished at the Electron Microscopy Platform of School of Physics and Information Technology, Shaanxi Normal University, Xi'an, China. This work was supported by the National Key Research and Development Project (2020YFC1521900 and 2020YFC1521904) and the National Natural Science Foundation of China (51802140 and 51672168).

Appendix A. Supporting information

Supplementary data associated with this article can be found in the online version at doi:10.1016/j.apcatb.2023.123464.

References

- [1] B. Yuan, X. Mao, Z. Wang, R. Hao, Y. Zhao, Radical-induced oxidation removal of multi-air-pollutant: a critical review, *J. Hazard. Mater.* 383 (2020), 121162.
- [2] X. Wen, X. Jiang, T. Jin, H. Chen, X. Zhang, S. Wang, Constructing oxygen vacancies on Bi_2MoO_6 nanosheets by aqueous ammonia etching with enhanced photocatalytic NO oxidation performance, *Energ. Fuel.* 36 (2022) 11485–11494.
- [3] N. Li, M. Shi, Y. Xin, W. Zhang, J. Qin, K. Zhang, H. Lv, M. Yuan, C. Wang, Oxygen vacancies-modified S-scheme $Bi_2Ti_2O_7/CaTiO_3$ heterojunction for highly efficient photocatalytic NO removal under visible light, *J. Environ. Chem. Eng.* 10 (2022), 107420.
- [4] Y. Dong, G. Li, D. Xu, Q. Wang, T. Yang, S. Pang, G. Zhang, L. Lv, Y. Xia, Z. Ren, P. Wang, A novel hierarchical heterostructure of hollow $La_2Ti_2O_7/In_2O_3$ with strong interface interaction for photocatalytic antibiotic degradation, *Chem. Eng. J.* 446 (2022), 136705.
- [5] H. Wu, R. Chen, H. Wang, W. Cui, J. Li, J. Wang, C. Yuan, L. Zhuo, Y. Zhang, F. Dong, An atomic insight into $BiOBr/La_2Ti_2O_7$ p-n heterojunctions: interfacial charge transfer pathway and photocatalysis mechanism, *Catal. Sci. Technol.* 10 (2020) 826–834.
- [6] L. Zhang, J. Zhang, H. Yu, J. Yu, Emerging S-scheme photocatalyst, *Adv. Mater.* 34 (2022), 2107668.
- [7] X. Wang, M. Sayed, O. Ruzimuradov, J. Zhang, Y. Fan, X. Li, X. Bai, J. Low, A review of step-scheme photocatalysts, *Appl. Mater. Today* 29 (2022), 101609.
- [8] F. Chang, X. Wang, C. Yang, S. Li, J. Wang, W. Yang, F. Dong, X. Hu, D.-g. Liu, Y. Kong, Enhanced photocatalytic NO removal with the superior selectivity for NO_2^-/NO_3^- species of $Bi_{12}GeO_{20}$ -based composites via a ball-milling treatment: Synergistic effect of surface oxygen vacancies and n-p heterojunctions, *Compos. Part B: Eng.* 231 (2022), 109600.

- [9] T. Cui, Y. Su, X. Fu, Y. Zhu, Y. Zhang, The key role of surface hydroxyls on the activity and selectivity in photocatalytic degradation of organic pollutants and NO_x removal, *J. Alloy. Compd.* 921 (2022), 165931.
- [10] H. Li, H. Shang, Y. Li, X. Cao, Z. Yang, Z. Ai, L. Zhang, Interfacial charging-decharging strategy for efficient and selective aerobic NO oxidation on oxygen vacancy, *Environ. Sci. Technol.* 53 (2019) 6964–6971.
- [11] M. Hojamberdiev, A. Yamaguchi, K. Yubuta, S. Oishi, K. Teshima, Fabrication of La₂Ti₂O₇ crystals using an alkali-metal molybdate flux growth method and their nitridability to form LaTiO₂N Crystals under a high-temperature NH₃ atmosphere, *Inorg. Chem.* 54 (2015) 3237–3244.
- [12] V. Tuyikeze, L.H. Omari, M. Bouhhou, A. Boudali, F. Fraija, Study of structural, and optical properties of the layered perovskite La₂Ti₂O₇ nanoparticle, *Mater. Today: Proc.* 30 (2020) 828–832.
- [13] E. Hua, S. Jin, X. Wang, S. Ni, G. Liu, X. Xu, Ultrathin 2D type-II p-n heterojunctions La₂Ti₂O₇/In₂S₃ with efficient charge separations and photocatalytic hydrogen evolution under visible light illumination, *Appl. Catal. B: Environ.* 245 (2019) 733–742.
- [14] X. Lin, H. Wang, H. Du, X. Xiong, B. Qu, Z. Guo, D. Chu, Growth of lithium lanthanum titanate nanosheets and their application in lithium-ion batteries, *ACS Appl. Mater. Inter.* 8 (2016) 1486–1492.
- [15] N.I. Ansari, P. Sivagnanapalani, V. Sureshkumar, B.W. Shivaraj, P.K. Panda, Synthesis of lanthanum titanate (La₂Ti₂O₇) for high temperature sensor applications, *J. Mater. Sci.: Mater. El.* 32 (2021) 27422–27428.
- [16] Y. Cao, P. Tang, Y. Han, W. Qiu, Synthesis of La₂Ti₂O₇ flexible self-supporting film and its application in flexible energy storage device, *J. Alloy. Compd.* 842 (2020), 155581.
- [17] S. Leroy, J.-F. Blach, M. Huvé, B. Léger, N. Kania, J.-F. Hennenot, A. Ponchel, S. Saitzek, Photocatalytic and sonophotocatalytic degradation of rhodamine B by nano-sized La₂Ti₂O₇ oxides synthesized with sol-gel method, *J. Photoch. Photobio. A* 401 (2020), 112767.
- [18] L. Lv, H.-D. Yang, H. Fan, L. Yang, Q.-W. Chen, J.-P. Zhou, La₂Ti₂O₇ nanosheets synthesized under magnetic field for ofloxacin ferrophotocatalytic degradation, *J. Environ. Chem. Eng.* 10 (2022), 108088.
- [19] X. Cai, L. Mao, M. Fujitsuka, T. Majima, S. Kasani, N. Wu, J. Zhang, Effects of Bi-dopant and co-catalysts upon hole surface trapping on La₂Ti₂O₇ nanosheet photocatalysts in overall solar water splitting, *Nano Res* 15 (2021) 438–445.
- [20] K. Das, D. Majhi, R. Bariki, B.G. Mishra, SnS₂/Bi₄Ti₃O₁₂ heterostructure material: A UV–visible light active direct Z-scheme photocatalyst for aqueous phase degradation of diazinon, *ChemistrySelect* 5 (2020) 1567–1577.
- [21] H. Shi, H. Tan, Z. W.-b. Zhu, Y. Sun, E. Ma, Wang, Electrospun Cr-doped Bi₄Ti₃O₁₂/Bi₂Ti₂O₇ heterostructure fibers with enhanced visible-light photocatalytic properties, *J. Mater. Chem. A* 3 (2015) 6586–6591.
- [22] Y. Ou, J. Shi, Q. Yan, C. Li, Y. Zheng, Ethanol-assisted molten salt synthesis of Bi₄Ti₃O₁₂/Bi₂Ti₂O₇ with enhanced visible light photocatalytic performance, *Inorg. Chem. Commun.* 133 (2021), 108867.
- [23] T. Cheng, Q. Ma, H. Gao, S. Meng, Z. Lu, S. Wang, Z. Yi, X. Wu, G. Liu, X. Wang, H. Yang, Enhanced photocatalytic activity, mechanism and potential application of I_{doped}-Bi₄Ti₃O₁₂ photocatalysts, *Mater. Today Chem.* 23 (2022), 100750.
- [24] G. Kresse, J. Furthmüller, Efficient iterative schemes for ab initio total-energy calculations using a plane-wave basis set, *Phys. Rev. B* 54 (1996) 11169–11186.
- [25] MedeaA, Materials Design, Inc.: Santa Fe, New Mexico, USA, 2013.
- [26] G. Kresse, D. Joubert, From ultrasoft pseudopotentials to the projector augmented-wave method, *Phys. Rev. B* 59 (1999) 1758–1775.
- [27] J.P. Perdew, K. Burke, M. Ernzerhof, Generalized gradient approximation made simple, *Phys. Rev. Lett.* 77 (1996) 3865–3868.
- [28] D.D. Ren, K.T. Gui, S.C. Gu, Y.L. Wei, Mechanism of improving the SCR NO removal activity of Fe₂O₃ catalyst by doping Mn, *J. Alloy. Compd.* 867 (2021), 158787.
- [29] C. Chen, Z. Gao, H. Yan, M.J. Reece, M.P. Paranthama, Crystallographic structure and ferroelectricity of [A_xLa_(1-x)]₂Ti₂O₇ (A = Sm and Eu) solid solutions with high T_c, *J. Am. Ceram. Soc.* 99 (2016) 523–530.
- [30] J. Xu, Y. Zhang, X. Xu, X. Fang, R. Xi, Y. Liu, R. Zheng, X. Wang, Constructing La₂B₂O₇ (B = Ti, Zr, Ce) compounds with three typical crystalline phases for the oxidative coupling of methane: The effect of phase structures, superoxide anions, and alkalinity on the reactivity, *ACS Catal.* 9 (2019) 4030–4045.
- [31] R. Swami, R. Bokolia, K. Sreenivas, Effects of sintering temperature on structural, electrical and ferroelectric properties of La₂Ti₂O₇ ceramics, *Ceram. Int.* 46 (2020) 26790–26799.
- [32] S.R. Das, P.S. Dabal, B. Sundarakannan, R.R. Das, R.S. Katiyar, Micro-Raman study of Zr-substituted Bi₄Ti₃O₁₂ ceramics, *J. Raman. Spectrosc.* 38 (2007) 1077–1081.
- [33] Z.C. Ling, H.R. Xia, W.L. Liu, H. Han, X.Q. Wang, S.Q. Sun, D.G. Ran, L.L. Yu, Lattice vibration of bismuth titanate nanocrystals prepared by metalorganic decomposition, *Mater. Sci. Eng.: B* 128 (2006) 156–160.
- [34] Y. Cui, P. Dang, F. Wang, P. Yuan, W. Liu, Y. Pu, Effect of oxygen vacancies on photoelectrochemical properties of amphoteric semiconductor Bi₄Ti₃O₁₂ photoelectrode, *Vacuum* 210 (2023), 111899.
- [35] X. Hu, J. Wang, J. Wang, Y. Deng, H. Zhang, T. Xu, W. Wang, β particles induced directional inward migration of oxygen vacancies: Surface oxygen vacancies and interface oxygen vacancies synergistically activate PMS, *Appl. Catal. B: Environ.* 318 (2022), 121879.
- [36] J. Qiu, D. Dai, L. Zhang, G. Xia, J. Yao, Oxygen vacancy-rich Bi₂MoO₆ anchored on cuboid metal-organic frameworks for photocatalytic elimination of Cr(VI)/2-nitrophenol mixed pollutants, *Sep. Purif. Technol.* 301 (2022), 121990.
- [37] T. Cheng, H. Gao, S. Wang, Z. Yi, G. Liu, Z. Pu, X. Wang, H. Yang, Surface doping of Bi₄Ti₃O₁₂ with S: enhanced photocatalytic activity, mechanism and potential photodegradation application, *Mater. Res. Bull.* 149 (2022), 111711.
- [38] T. Cheng, H. Gao, G. Liu, Z. Pu, S. Wang, Z. Yi, X. Wu, H. Yang, Preparation of core-shell heterojunction photocatalysts by coating CdS nanoparticles onto Bi₄Ti₃O₁₂ hierarchical microspheres and their photocatalytic removal of organic pollutants and Cr(VI) ions, *Colloids Surf. A: Physicochem. Eng. Asp.* 633 (2022), 127918.
- [39] S. Niu, R. Zhang, X. Zhang, J. Xiang, C. Guo, Morphology-dependent photocatalytic performance of Bi₄Ti₃O₁₂, *Ceram. Int.* 46 (2020) 6782–6786.
- [40] Y. Zhou, Q. Li, J. Zhang, M. Xiang, Y. Zhou, Z. Chen, Y. Chen, T. Yao, Broad spectrum driven Y doped BiO_{2-x} for enhanced degradation of tetracycline: synergy between singlet oxygen and free radicals, *Appl. Surf. Sci.* 607 (2023), 154957.
- [41] M. Arif, M. Zhang, Y. Mao, Q. Bu, A. Ali, Z. Qin, T. Muhmood, X. Shahnoor, B. Liu, S.M. Zhou, Chen, Oxygen vacancy mediated single unit cell Bi₂WO₆ by Ti doping for ameliorated photocatalytic performance, *J. Colloid Interf. Sci.* 581 (2021) 276–291.
- [42] G. Xu, Y. Yang, H. Bai, J. Wang, H. Tian, R. Zhao, X. Wei, X. Yang, G. Han, Hydrothermal synthesis and formation mechanism of the single-crystalline Bi₄Ti₃O₁₂ nanosheets with dominant (010) facets, *CrystEngComm* 18 (2016) 2268–2274.
- [43] D. Makovec, N. Krizaj, S. Gyergyek, Hydrothermal formation of bismuth-titanate nanoparticles and nanowires: the role of metastable polymorphs, *CrystEngComm* 24 (2022) 3972–3981.
- [44] Z. Huang, J. Liu, L. Huang, L. Tian, W. Sen, G. Zhang, J. Li, F. Liang, H. Zhang, Q. Jia, S. Zhang, One-step synthesis of dandelion-like lanthanum titanate nanostructures for enhanced photocatalytic performance, *NPG Asia Mater.* 12 (2020) 11.
- [45] X. Cai, M. Zhu, O.A. Elbanna, M. Fujitsuka, S. Kim, L. Mao, J. Zhang, T. Majima, Au nanorod photosensitized La₂Ti₂O₇ nanosteps: successive surface heterojunctions boosting visible to near-infrared photocatalytic H₂ evolution, *ACS Catal.* 8 (2018) 122–131.
- [46] S. Wei, Y. Chen, P. Wu, X. Liu, J. Ren, B. Yao, H. Xu, W. Dou, Y. Wang, R. Wu, Z. Fang, Q. Liang, Surface defects engineered Bi₄Ti₃O₁₂ nanosheets for photocatalytic degradation of antibiotic levofloxacin, *Appl. Catal. A: Gen.* 640 (2022), 118675.
- [47] G.A.S. Alves, H.A. Centurion, J.R. Sambrano, M.M. Ferrer, R.V. Gonçalves, Band gap narrowing of Bi-doped NaTaO₃ for photocatalytic hydrogen evolution under simulated sunlight: A pseudocubic phase induced by doping, *ACS Appl. Energy Mater.* 4 (2020) 671–679.
- [48] F. Zhang, Y. Xu, H. Yang, S. Guan, W. Shi, Y. Chen, C. Huang, J. Xing, H. Liu, Q. Chen, Effects of cerium on structures and electrical properties of (Nb, Ta) modified Bi₄Ti₃O₁₂, piezoelectric Ceramics, *J. Am. Ceram. Soc.* 105 (2022) 4161–4170.
- [49] Z. Ma, Y. Li, Y. Lv, R. Sa, Q. Li, K. Wu, Synergistic effect of doping and compositing on photocatalytic efficiency: a case study of La₂Ti₂O₇, *ACS Appl. Mater. Inter.* 10 (2018) 39327–39335.
- [50] Z. Liu, Z. Ma, Promoting the photocatalytic activity of Bi₄Ti₃O₁₂ microspheres by incorporating iron, *RSC Adv.* 10 (2020) 19232–19239.
- [51] X. Feng, B. Lv, L. Lu, X. Feng, H. Wang, B. Xu, Y. Yang, F. Zhang, Role of surface oxygen vacancies in zinc oxide/graphitic carbon nitride composite for adjusting energy band structure to promote visible-light-driven photocatalytic activity, *Appl. Surf. Sci.* 562 (2021), 150106.
- [52] R. López, R. Gómez, Band-gap energy estimation from diffuse reflectance measurements on sol-gel and commercial TiO₂: a comparative study, *J. Sol. -gel. Sci. Techn.* 61 (2011) 1–7.
- [53] K. Gelderman, L. Lee, S.W. Donne, Flat-band potential of a semiconductor: using the Mott-Schottky, *Equ., J. Chem. Educ.* 84 (2007) 685.
- [54] Y. Li, R. Li, Y. Zhai, Y. Huang, S. Lee, J. Cao, Improved photocatalytic activity of BaTiO₃/La₂Ti₂O₇ heterojunction composites via piezoelectric-enhanced charge transfer, *Appl. Surf. Sci.* 570 (2021), 151146.
- [55] Y. Duan, J. Luo, S. Zhou, X. Mao, M.W. Shah, F. Wang, Z. Chen, C. Wang, TiO₂-supported Ag nanoclusters with enhanced visible light activity for the photocatalytic removal of NO, *Appl. Catal. B: Environ.* 234 (2018) 206–212.
- [56] Y. Lu, Y. Huang, Y. Zhang, J.-j. Cao, H. Li, C. Bian, S. C. Lee, Oxygen vacancy engineering of Bi₂O₃/Bi₂O₂CO₃ heterojunctions: Implications of the interfacial charge transfer, NO adsorption and removal, *Appl. Catal. B: Environ.* 231 (2018) 357–367.
- [57] P. Zhao, N. Feng, F. Fang, H. Wan, G. Guan, Surface acid etching for efficient anchoring of potassium on 3DOM La_{0.8}Sr_{0.2}MnO₃ catalyst: an integration strategy for boosting soot and NO_x simultaneous elimination, *J. Hazard. Mater.* 409 (2021), 124916.
- [58] Y. Deng, Z. Zhou, H. Zeng, R. Tang, L. Li, J. Wang, C. Feng, D. Gong, L. Tang, Y. Huang, Phosphorus and potassium co-doped g-C₃N₄ with multiple-locus synergies to degrade atrazine: Insights into the depth analysis of the generation and role of singlet oxygen, *Appl. Catal. B: Environ.* 320 (2023), 121942.
- [59] W. Zhang, J. Zhao, A.A. Allam, Y. Xin, J. Lin, T. Gao, J.S. Ajarem, X. Li, C. Wang, D. W. Bahnemann, Palladium nanoparticles embedded nutshell-like Bi₂WO₆ as an efficient and stable visible-light-responsive photocatalysts for NO removal, *Energ. Fuel.* 36 (2022) 13852–13862.
- [60] Y. Xin, Q. Zhu, T. Gao, X. Li, W. Zhang, H. Wang, D. Ji, Y. Huang, M. Padervand, F. Yu, C. Wang, Photocatalytic NO removal over defective Bi/BiOBr nanoflowers: The inhibition of toxic NO₂ intermediate via high humidity, *Appl. Catal. B: Environ.* 324 (2023), 122238.
- [61] K. Li, W. Zhou, X. Li, Q. Li, S.A.C. Carabineiro, S. Zhang, J. Fan, K. Lv, Synergistic effect of cyano defects and CaCO₃ in graphitic carbon nitride nanosheets for efficient visible-light-driven photocatalytic NO removal, *J. Hazard. Mater.* 442 (2023), 130040.

- [62] Y. Sun, H. Wang, Q. Xing, W. Cui, J. Li, S. Wu, L. Sun, The pivotal effects of oxygen vacancy on Bi_2MoO_6 : promoted visible light photocatalytic activity and reaction mechanism, Chinese, J. Catal. 40 (2019) 647–655.
- [63] X. Xie, Q.-U. Hassan, H. Lu, F. Rao, J. Gao, G. Zhu, In situ construction of oxygen-vacancy-rich $\text{BiO@Bi}_2\text{WO}_6$ microspheres with enhanced visible light photocatalytic for NO removal, Chinese, Chem. Lett. 32 (2021) 2038–2042.
- [64] Y. Huang, Y. Gao, Q. Zhang, J.-j. Cao, R.-j. Huang, W. Ho, S.C. Lee, Hierarchical porous ZnWO_4 microspheres synthesized by ultrasonic spray pyrolysis: Characterization, mechanistic and photocatalytic NO removal studies, Appl. Catal. A: Gen. 515 (2016) 170–178.
- [65] F. Rao, G. Zhu, W. Zhang, Y. Xu, B. Cao, X. Shi, J. Gao, Y. Huang, Y. Huang, M. Hojamberdiev, Maximizing the formation of reactive oxygen species for deep oxidation of NO via manipulating the oxygen-vacancy defect position on $(\text{BiO})_2\text{CO}_3$, ACS Catal. 11 (2021) 7735–7749.
- [66] K. Qi, J. Jing, G. Dong, P. Li, Y. Huang, The excellent photocatalytic NO removal performance relates to the synergistic effect between the prepositive NaOH solution and the g- C_3N_4 photocatalysis, Environ. Res. 212 (2022), 113405.
- [67] Z. Wang, Y. Huang, M. Chen, X. Shi, Y. Zhang, J. Cao, W. Ho, S.C. Lee, Roles of N-vacancies over porous g- C_3N_4 microtubes during photocatalytic NO_x removal, ACS Appl. Mater. Inter. 11 (2019) 10651–10662.
- [68] J. Geng, L. Zhao, M. Wang, G. Dong, W. Ho, The photocatalytic NO-removal activity of g- C_3N_4 significantly enhanced by the synergistic effect of Pd^0 nanoparticles and N vacancies, Environ. Sci.: Nano 9 (2022) 742–750.
- [69] X. Hu, Y. Wang, Z. Ling, H. Song, Y. Cai, Z. Li, D. Zu, C. Li, Ternary g- $\text{C}_3\text{N}_4/\text{TiO}_2/\text{Ti}_3\text{C}_2$ MXene S-scheme heterojunction photocatalysts for NO_x removal under visible light, Appl. Surf. Sci. 556 (2021), 149817.
- [70] F. Chang, C. Yang, J. Wang, B. Lei, S. Li, H. Kim, Enhanced photocatalytic conversion of NO_x with satisfactory selectivity of $^3\text{D}-^2\text{D}$ $\text{Bi}_4\text{O}_5\text{Br}_2$ -GO hierarchical structures via a facile microwave-assisted preparation, Sep. Purif. Technol. 266 (2021), 118237.
- [71] Y. Ou, G. Zhu, F. Rao, J. Gao, J. Chang, X. Xie, W. Zhang, Y. Huang, M. Hojamberdiev, Coral-shaped TiO_2 -8 decorated with carbon quantum dots and carbon nanotubes for NO removal, ACS Appl. Nano Mater. 4 (2021) 7330–7342.
- [72] X. Shi, P. Wang, W. Li, Y. Bai, H. Xie, Y. Zhou, L. Ye, Change in photocatalytic NO removal mechanisms of ultrathin BiOBr/BiOI via NO_3^- adsorption, Appl. Catal. B: Environ. 243 (2019) 322–329.
- [73] J. Li, M. Ran, P. Chen, W. Cui, J. Li, Y. Sun, G. Jiang, Y. Zhou, F. Dong, Controlling the secondary pollutant on B-doped g- C_3N_4 during photocatalytic NO removal: a combined DRIFTS and DFT investigation, Catal. Sci. Technol. 9 (2019) 4531–4537.
- [74] N. Tang, Y. Liu, H. Wang, Z. Wu, Mechanism study of NO catalytic oxidation over $\text{MnO}_x/\text{TiO}_2$, Catal., J. Phys. Chem. C. 115 (2011) 8214–8220.
- [75] G. Jiang, X. Li, M. Lan, T. Shen, X. Lv, F. Dong, S. Zhang, Monodisperse bismuth nanoparticles decorated graphitic carbon nitride: Enhanced visible-light-response photocatalytic NO removal and reaction pathway, Appl. Catal. B: Environ. 205 (2017) 532–540.
- [76] G. Li, B. Wang, Z. Wang, Z. Li, Q. Sun, W.Q. Xu, Y. Li, Reaction mechanism of low-temperature selective catalytic reduction of NO_x over Fe-Mn oxides supported on fly-ash-derived SBA-15 molecular sieves: structure-activity relationships and in situ DRIFT analysis, J. Phys. Chem. C. 122 (2018) 20210–20231.